CMS Physics Analysis Summary

Contact: cms-pag-conveners-susy@cern.ch 2019/03/19

Searches for new phenomena in events with jets and high values of the M_{T2} variable, including signatures with disappearing tracks, in proton-proton collisions at $\sqrt{s} = 13$ TeV

The CMS Collaboration

Abstract

Searches for new phenomena are performed using events with jets and significant transverse momentum imbalance. In events with at least two jets, the transverse momentum imbalance is inferred through the M_{T2} variable. The results are based on a sample of proton-proton collisions collected with the CMS detector during the LHC Run II (2016-2018) and correspond to an integrated luminosity of 137 fb^{-1} taken at a center-of-mass energy of 13 TeV. Two related searches are performed. The first is an inclusive search based on signal regions defined by the hadronic energy in the event, the jet multiplicity, the number of jets identified as originating from bottom quarks, and the value of M_{T2} for events with at least two jets, or the tranverse momentum of the jet for events with just one jet. The second is a search for disappearing tracks produced by new long-lived charged particles, decaying within the volume of the CMS tracking detector. No excess event yield is observed above the predicted standard model background, leading to exclusion limits on pair-produced gluinos and squarks in simplified models of R-parity conserving supersymmetry. Mass limits as high as 2250 GeV, 1770 GeV, 1260 GeV and 1225 GeV are obtained from the inclusive M_{T2} search for gluinos, light-flavor squarks, bottom squarks and top squarks, respectively. The search for disappearing tracks extends the gluino mass limit to as much as 2460 GeV, and the $\tilde{\chi}_1^0$ mass limit to as much as 2000 GeV, in models where the gluino can decay with equal probability to $\tilde{\chi}_1^0$, $\tilde{\chi}_1^+$, and $\tilde{\chi}_1^-$, and the $\tilde{\chi}_1^\pm$ are long-lived.

1 Introduction

We present results of two related searches for new phenomena in events with jets and significant transverse momentum imbalance, based on a data set of proton-proton collisions collected with the CMS detector during the LHC Run II (2016–2018), corresponding to an integrated luminosity of 137 fb^{-1} taken at $\sqrt{s} = 13\,\text{TeV}$.

The first one is an inclusive search, and exploits the transverse momentum imbalance as inferred through the M_{T2} variable [1–5], defined in Sec. 3.1, in events with at least two jets, or the transverse momentum of the jet in events with just one jet. Similar searches were previously conducted by both the ATLAS [6–11] and CMS [2, 12–15] Collaborations. Our search builds on the work presented in Refs. [2, 12], using improved methods to estimate the background from standard model (SM) processes. Event counts in bins of the number of jets (N_{j}), the number of b-tagged jets (N_{b}), the scalar sum of the transverse momenta p_{T} of all selected jets (H_{T}), and the M_{T2} variable if $N_{\text{j}} \geq 2$, or the transverse momentum of the jet if $N_{\text{j}} = 1$, are compared against estimates of the background from SM processes derived from dedicated data control samples.

The second search aims at extending the sensitivity of the former one towards scenarios where the mass spectrum of potential new particles is compressed. In such scenarios, theories [16, 17] foresee the presence of new long-lived charged particles, that can be identified as *disappearing tracks* when they decay within the volume of the tracking detector. This search exploits the presence of disappearing tracks in order to suppress the background from SM processes, and to enhance the sensitivity towards these scenarios. Similar searches were previously conducted by both the ATLAS [18] and CMS [19–21] Collaborations. Our search uses events with at least two jets, and the M_{T2} variable to further suppress the background from SM processes.Event counts in bins of N_{j}, H_{T}, disappearing track length, and disappearing track p_{T} are compared against estimates of the background from SM processes derived from dedicated data control samples.

We observe no evidence for a significant excess above the expected background event yield and interpret the results as exclusion limits at 95% confidence level on pair-produced gluinos and squarks in simplified models of R-parity conserving supersymmetry (SUSY) [22–29].

2 The CMS detector

The central feature of the CMS apparatus is a superconducting solenoid of 6 m internal diameter, providing a magnetic field of 3.8 T. Within the solenoid volume are a silicon pixel and strip tracker, a lead tungstate crystal electromagnetic calorimeter, and a brass and scintillator hadron calorimeter, each composed of a barrel and two endcap sections. Forward calorimeters extend the pseudorapidity (η) coverage provided by the barrel and endcap detectors. Muons are measured in gas-ionization detectors embedded in the steel flux-return yoke outside the solenoid. The first level of the CMS trigger system, composed of custom hardware processors, uses information from the calorimeters and muon detectors to select the most interesting events in a fixed time interval of less than 4 μs. The high-level trigger processor farm further decreases the event rate from around 100 kHz to less than 1 kHz, before data storage. A more detailed description of the CMS detector and trigger system, together with a definition of the coordinate system used and the relevant kinematic variables, can be found in Refs. [30, 31].

3 Event selection and Monte Carlo simulation

3.1 Event selection

Events are processed using the particle-flow (PF) algorithm [32], which is designed to reconstruct and identify all particles using the optimal combination of information from the elements of the CMS detector. The physics objects reconstructed with this algorithm are hereafter referred to as particle-flow candidates. The physics objects and the event preselection are similar to those described in Ref. [2], and are summarized in Table 1 and are described in detail below. We select events with at least one jet, and veto events with an isolated lepton (e or μ) or charged PF candidate. The isolated charged PF candidate selection is designed to provide additional rejection against events with electrons and muons, as well as to reject hadronic tau decays. Jets are formed by clustering PF candidates using the anti-k_{T} algorithm [33, 34] and are corrected for contributions from event pileup [35] and the effects of non-uniform detector response. Only jets passing the selection criteria in Table 1 are used for counting and the determination of kinematic variables. Jets consistent with originating from a heavy-flavor hadron are identified using a deep neural network algorithm [36], with a working point chosen such that the efficiency to identify a b quark jet is in the range 55–70% for jet p_{T} between 20 and 400 GeV. The misidentification rate is approximately 1–2% for light-flavor and gluon jets and 10–15% for charm jets.

The negative of the vector sum of the p_{T} of all selected jets is denoted by $\vec{H}_{\mathrm{T}}^{\mathrm{miss}}$, while $\vec{p}_{\mathrm{T}}^{\mathrm{miss}}$ is defined as the negative of the vector p_{T} sum of all reconstructed PF candidates. The jet corrections are also used to correct $\vec{p}_{\mathrm{T}}^{\mathrm{miss}}$. Events with possible contributions from beam-halo processes or anomalous noise in the calorimeter are rejected using dedicated filters [37, 38]. For events with at least two jets, we start with the pair having the largest dijet invariant mass and iteratively cluster all selected jets using an algorithm that minimizes the Lund distance measure [39, 40] until two stable pseudo-jets are obtained. The resulting pseudo-jets together with the $\vec{p}_{\mathrm{T}}^{\mathrm{miss}}$ are used to calculate the kinematic variable M_{T2} [1] as:

$$M_{\mathrm{T2}} = \min_{\vec{p}_{\mathrm{T}}^{\mathrm{miss\,X}(1)}+\vec{p}_{\mathrm{T}}^{\mathrm{miss\,X}(2)}=\vec{p}_{\mathrm{T}}^{\mathrm{miss}}} \left[\max\left(M_{\mathrm{T}}^{(1)}, M_{\mathrm{T}}^{(2)}\right)\right], \tag{1}$$

where $\vec{p}_{\mathrm{T}}^{\mathrm{miss\,X}(i)}$ ($i = 1,2$) are trial vectors obtained by decomposing $\vec{p}_{\mathrm{T}}^{\mathrm{miss}}$, and $M_{\mathrm{T}}^{(i)}$ are the transverse masses [41] obtained by pairing either of the trial vectors with one of the two pseudo-jets. The minimization is performed over all trial momenta satisfying the $\vec{p}_{\mathrm{T}}^{\mathrm{miss}}$ constraint. The background from multijet events (discussed in Sec. 4) is characterized by small values of M_{T2}, while larger M_{T2} values are obtained in processes with significant, genuine $\vec{p}_{\mathrm{T}}^{\mathrm{miss}}$. A more detailed description of the M_{T2} properties is given in Refs. [3–5].

In both the inclusive M_{T2} search and the search for disappearing tracks, collision events are selected using triggers with requirements on H_{T}, $p_{\mathrm{T}}^{\mathrm{miss}}$, $H_{\mathrm{T}}^{\mathrm{miss}}$, and jet p_{T}. The combined trigger efficiency, as measured in a data sample of events with an isolated electron, is found to be $>$97% across the full kinematic range of the search. To suppress background from multijet production, we require $M_{\mathrm{T2}} > 200$ GeV in events with $N_{\mathrm{j}} \geq 2$. In the inclusive M_{T2} search, this M_{T2} threshold is increased to 400 GeV for events with $H_{\mathrm{T}} > 1500$ GeV to maintain multijet processes as a subdominant background in all search regions. To protect against jet mismeasurement, we require the minimum difference in azimuthal angle between the $\vec{p}_{\mathrm{T}}^{\mathrm{miss}}$ vector and each of the leading four jets, $\Delta\phi_{\mathrm{min}}$, to be greater than 0.3, and the magnitude of the difference between $\vec{p}_{\mathrm{T}}^{\mathrm{miss}}$ and $\vec{H}_{\mathrm{T}}^{\mathrm{miss}}$ to be less than half of $p_{\mathrm{T}}^{\mathrm{miss}}$. For the determination of $\Delta\phi_{\mathrm{min}}$ we consider jets with $|\eta| < 4.7$. If less than four such jets are found, all are considered in the $\Delta\phi_{\mathrm{min}}$ calculation.

Table 1: Summary of the trigger requirements and the kinematic offline event preselection requirements on the reconstructed physics objects, for both the inclusive M_{T2} search and the search for disappearing tracks. Here R is the distance parameter of the anti-k_T algorithm. For veto leptons and tracks, the transverse mass M_T is determined using the veto object and the $\vec{p}_T^{\,miss}$. The variable p_T^{sum} is a measure of isolation and it denotes the sum of the transverse momenta of all the PF candidates in a cone around the lepton or the track. The size of the cone, in units of $\Delta R \equiv \sqrt{(\Delta\phi)^2 + (\Delta\eta)^2}$ is given in the table. Further details of the lepton selection are described in Refs. [2, 3]. The ith highest-p_T jet is denoted as j_i.

Trigger	2016: $p_T^{miss} > 120\,GeV$ and $H_T^{miss} > 120\,GeV$ or $H_T > 300\,GeV$ and $p_T^{miss} > 110\,GeV$ or $H_T > 900\,GeV$ or jet $p_T > 450\,GeV$ 2017 and 2018: $p_T^{miss} > 120\,GeV$ and $H_T^{miss} > 120\,GeV$ or $H_T > 60\,GeV$ and $p_T^{miss} > 120\,GeV$ and $H_T^{miss} > 120\,GeV$ or $H_T > 500\,GeV$ and $p_T^{miss} > 100\,GeV$ and $H_T^{miss} > 100\,GeV$ or $H_T > 800\,GeV$ and $p_T^{miss} > 75\,GeV$ and $H_T^{miss} > 75\,GeV$ or $H_T > 1050\,GeV$ or jet $p_T > 500\,GeV$
Jet selection	$R = 0.4$, $p_T > 30\,GeV$, $\lvert\eta\rvert < 2.4$
b tag selection	$p_T > 20\,GeV$, $\lvert\eta\rvert < 2.4$
p_T^{miss}	$p_T^{miss} > 250\,GeV$ for $H_T < 1200\,GeV$, else $p_T^{miss} > 30\,GeV$ $\Delta\phi_{min} = \Delta\phi\left(p_T^{miss}, j_{1,2,3,4}\right) > 0.3$ $\lvert\vec{p}_T^{\,miss} - \vec{H}_T^{miss}\rvert / p_T^{miss} < 0.5$
M_{T2}	Inclusive M_{T2} search (if $N_j \geq 2$): $M_{T2} > 200\,GeV$ for $H_T < 1500\,GeV$, else $M_{T2} > 400\,GeV$ Search for disappearing tracks (if $N_j \geq 2$): $M_{T2} > 200\,GeV$
Veto muon	$p_T > 10\,GeV$, $\lvert\eta\rvert < 2.4$, $p_T^{sum} < 0.2\,p_T^{lep}$
Veto muon track	$p_T > 5\,GeV$, $\lvert\eta\rvert < 2.4$, $M_T < 100\,GeV$, $p_T^{sum} < 0.2\,p_T^{lep}$
Veto electron	$p_T > 10\,GeV$, $\lvert\eta\rvert < 2.4$, $p_T^{sum} < 0.1\,p_T^{lep}$
Veto electron track	$p_T > 5\,GeV$, $\lvert\eta\rvert < 2.4$, $M_T < 100\,GeV$, $p_T^{sum} < 0.2\,p_T^{lep}$
Veto track	$p_T > 10\,GeV$, $\lvert\eta\rvert < 2.4$, $M_T < 100\,GeV$, $p_T^{sum} < 0.1\,p_T^{track}$
p_T^{sum} cone (isolation)	Veto e or μ: $\Delta R = \min(0.2, \max(10\,GeV/p_T^{lep}, 0.05))$ Veto track: $\Delta R = 0.3$

In the search for disappearing tracks, events are selected requiring the presence of at least one disappearing track. A disappearing track is identified as a well reconstructed isolated track, disappearing within the volume of the CMS tracking detector. To ensure this, we require the presence of at least two outer layers of the tracking detector without a measurement. Because the track disappears within the tracking detector and is not associated to any energy deposits in the calorimeters, the track itself is not reconstructed as a PF candidate, and therefore is not accounted for in the calculation of $\vec{p}_{\mathrm{T}}^{\,\mathrm{miss}}$. In the following, the selected disappearing tracks are called *short tracks* (ST). We also define *short track candidates* (STC), as disappearing tracks that are required to satisfy relaxed selections compared to an ST, and to not be an ST.

3.2 Event categorization

3.2.1 Inclusive M_{T2} search

Events containing at least two jets are categorized by the values of N_{j}, N_{b}, and H_{T}. Each such bin is referred to as a *topological region*. Signal regions are defined by further dividing topological regions into bins of M_{T2}. Events with only one jet are selected if the p_{T} of the jet is at least 250 GeV, and are classified according to the p_{T} of this jet and whether the event contains a b-tagged jet. The search regions are summarized in Tables 4-6 in Appendix B.1.

3.2.2 Search for disappearing tracks

Events containing at least one ST and at least two jets are selected, and categorized by the values of N_{j} and H_{T}. In each such bin, disappearing tracks are further categorized according to their length and p_{T}. Two bins of p_{T} are defined:

- $15 < p_{\mathrm{T}} < 50$ GeV.
- $p_{\mathrm{T}} > 50$ GeV.

Additionally, four track length categories are defined, depending on the number of layers of the tracking detector with a measurement:

- pixel tracks (P), with all (at least three) layers with a measurement belonging to CMS pixel tracking detector.
- medium length tracks (M), with less than seven layers with a measurement, and at least one outside of the pixel tracking detector.
- long tracks (L), with at least seven layers with a measurement.

In 2017 and 2018, we further split the P tracks into two categories:

- pixel tracks with three layers with a measurement (P3).
- pixel tracks with at least four layers with a measurement (P4).

For long (L) tracks, no categorization in bins of p_{T} is applied.

We adopt such categorization for two main reasons: to maximize sensitivity to a wider range of lifetimes of potential new long-lived charged particles, and to distinguish tracks reconstructed with different precision. The full track selection requirements, that depend on the track length category, are listed in Table 3 of Appendix A. The search regions are summarized in Tables 7–8 in Appendix B.2.

3.3 Monte Carlo simulation

Monte Carlo (MC) simulations are used to design the search, to aid in the estimation of SM backgrounds, and to evaluate the sensitivity to gluino and squark pair production in simplified models of SUSY. The main background samples (Z+jets, W+jets, and $\mathrm{t\bar{t}}$+jets), as well as signal samples of gluino and squark pair production, are generated at leading order (LO) precision with the MADGRAPH 5 generator [42, 43] interfaced with PYTHIA 8.2 [44] for fragmentation and parton showering. Up to four, three, or two additional partons are considered in the matrix element calculations for the generation of the V+jets ($\mathrm{V} = \mathrm{Z}, \mathrm{W}$), $\mathrm{t\bar{t}}$+jets, and signal samples, respectively. Other background processes are also considered: $\mathrm{t\bar{t}V}(\mathrm{V} = \mathrm{Z}, \mathrm{W})$ samples are generated at LO precision with the MADGRAPH 5 generator, with up to two additional partons in the matrix element calculations, while single top samples are generated at next-to-leading order (NLO) precision with the MADGRAPH_aMC@NLO [42] or POWHEG [45, 46] generators. Finally, contributions from rarer processes such as diboson, triboson, and four top production, are as well considered, and found to be negligible. Standard model samples are simulated with a detailed GEANT4 [47] based detector simulation and processed using the same chain of reconstruction programs as collision data, while the CMS fast simulation program [48] is used for the signal samples. The most precise available cross section calculations are used to normalize the simulated samples, corresponding most often to NLO or next-to-NLO accuracy [45, 46, 49–53].

To improve on the MADGRAPH modeling of the multiplicity of additional jets from initial state radiation (ISR), MADGRAPH $\mathrm{t\bar{t}}$ MC events in 2016 are weighted based on the number of ISR jets ($N_{\mathrm{j}}^{\mathrm{ISR}}$) so as to make the jet multiplicity agree with data. The same reweighting procedure is applied to SUSY MC events. The weighting factors are obtained from a control region enriched in $\mathrm{t\bar{t}}$, obtained by selecting events with two leptons and exactly two b-tagged jets, and vary between 0.92 for $N_{\mathrm{j}}^{\mathrm{ISR}} = 1$ and 0.51 for $N_{\mathrm{j}}^{\mathrm{ISR}} \geq 6$. We take one half of the deviation from unity as the systematic uncertainty in these reweighting factors, to cover for differences between $\mathrm{t\bar{t}}$ and SUSY production. Thanks to a better tuning of the MC generators, this reweighting procedure is not necessary in 2017 and 2018 MC events. To improve the modeling of the flavor of additional jets, the simulation of $\mathrm{t\bar{t}}$ and $\mathrm{t\bar{t}V}(\mathrm{V} = \mathrm{Z}, \mathrm{W})$ events in 2016, 2017, and 2018 is also corrected to account for the measured ratio of $\mathrm{t\bar{t}b\bar{b}}/\mathrm{t\bar{t}jj}$ cross sections reported in Ref. [54]. Simulated $\mathrm{t\bar{t}}$ and $\mathrm{t\bar{t}V}(\mathrm{V} = \mathrm{Z}, \mathrm{W})$ events with two b quarks not originating from top quark decay are weighted to account for the CMS measurement of the ratio of cross sections $\sigma(\mathrm{t\bar{t}b\bar{b}})/\sigma(\mathrm{t\bar{t}jj})$, which was found to be a factor of 1.7 ± 0.5 larger than the MC prediction [54]. A systematic uncertainty is assessed, to cover for the effect of the variations of such reweighting factor by the associated uncertainty.

4 Backgrounds

4.1 Inclusive M_{T2} search

The backgrounds in jets-plus-$p_{\mathrm{T}}^{\mathrm{miss}}$ final states typically arise from three categories of SM processes:

- *lost lepton* (LL), i.e., events with a lepton from a W decay where the lepton is either out of acceptance, not reconstructed, not identified, or not isolated. This background originates mostly from W+jets and $\mathrm{t\bar{t}}$+jets events, with smaller contributions from rarer processes such as diboson or $\mathrm{t\bar{t}V}(\mathrm{V} = \mathrm{Z}, \mathrm{W})$ production.
- *irreducible*, i.e., Z+jets events, where the Z boson decays to neutrinos. This background is most similar to potential signals. It is a major background in nearly all

search regions, its importance decreasing with increasing N_b.

- *instrumental background*, i.e., mostly multijet events with no genuine p_T^{miss}. These events enter a search region due to either significant jet momentum mismeasurements, or sources of anomalous noise.

4.1.1 Estimation of the background from events with leptonic W boson decays

The *lost lepton* background is estimated from control regions with exactly one lepton candidate selected using the same triggers and preselections used for the signal regions, with the exception of the lepton veto, which is inverted. Selected events are binned according to the same criteria as the search regions, and the background in each signal bin, N_{LL}^{SR}, is obtained from the number of events in the control region, $N_{1\ell}^{CR}$, using transfer factors according to:

$$N_{LL}^{SR}\left(H_T, N_j, N_b, M_{T2}\right) = N_{1\ell}^{CR}\left(H_T, N_j, N_b, M_{T2}\right) R_{MC}^{0\ell/1\ell}\left(H_T, N_j, N_b, M_{T2}\right) k_{LL}\left(M_{T2}\right). \quad (2)$$

The single-lepton control region typically has 1–2 times as many events as the corresponding signal region. The factor $R_{MC}^{0\ell/1\ell}\left(H_T, N_j, N_b, M_{T2}\right)$ accounts for lepton acceptance and efficiency and the expected contribution from the decay of W bosons to hadrons through an intermediate τ lepton. It is obtained from MC simulation, and corrected for measured differences in lepton efficiencies between data and simulation.

The factor $k_{LL}\left(M_{T2}\right) = 1$, except for events with $N_j \geq 2$ at high M_{T2} values, where the single-lepton control sample has insufficient statistics to allow $N_{1\ell}^{CR}$ to be measured in each (H_T, N_j, N_b, M_{T2}) bin. In such cases, $N_{1\ell}^{CR}$ is only binned in (H_T, N_j, N_b) and the distribution in M_{T2} inside each (H_T, N_j, N_b) bin is taken from simulation, applied through the factor $k_{LL}\left(M_{T2}\right)$. The modeling of M_{T2} is checked in data, in single-lepton events with either $N_b = 0$ or $N_b \geq 1$, as shown in the left and right panels of Fig. 1, respectively. The predicted distributions in the comparison are obtained by summing all the relevant regions, after normalizing MC yields to data and distributing events among M_{T2} bins according to the expectation from simulation. For events with $N_j = 1$, no distribution among M_{T2} bins is necessary.

Uncertainties from the limited size of the control sample and from theoretical and experimental quantities are evaluated and propagated to the final estimate. The dominant uncertainty in $R_{MC}^{0\ell/1\ell}\left(H_T, N_j, N_b, M_{T2}\right)$ arises from the modeling of the lepton efficiency (for electrons, muons, and hadronically-decaying tau leptons) and jet energy scale (JES) and is of order 15–20%. The uncertainty in the M_{T2} extrapolation via $k_{LL}\left(M_{T2}\right)$, which is as large as 40%, arises primarily from the JES, the relative fractions of W+jets and $t\bar{t}$+jets, and variations of the renormalization and factorization scales assumed for their simulation.

4.1.2 Estimation of the background from $Z(\nu\bar{\nu})$+jets

The $Z \to \nu\bar{\nu}$ background is estimated from a dilepton control sample selected using triggers requiring two leptons. The trigger efficiency, measured with a data sample of events with large H_T, is found to be greater than 97% in the selected kinematic range. To obtain a control sample enriched in $Z \to \ell^+\ell^-$ events ($\ell = e, \mu$), we require that the leptons are of the same flavor, opposite charge, that the p_T of the leading and trailing leptons are at least 100 GeV and 30 GeV, respectively, and that the invariant mass of the lepton pair is consistent with the mass of a Z boson within 20 GeV. After requiring that the p_T of the dilepton system is at least 200 GeV, the preselection requirements are applied based on kinematic variables recalculated after removing the dilepton system from the event to replicate the $Z \to \nu\bar{\nu}$ kinematics. For events with $N_j = 1$,

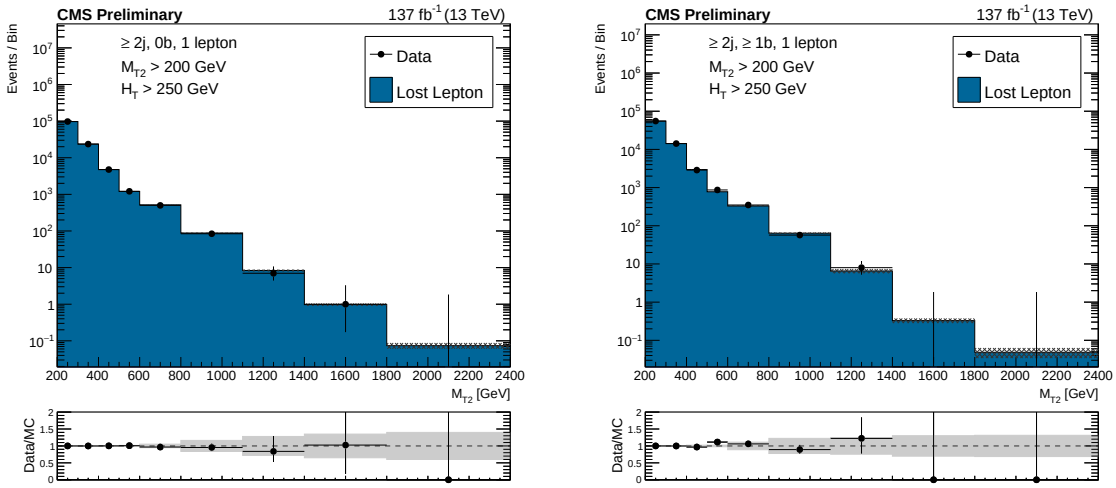

Figure 1: Distributions of the M_{T2} variable in data and simulation for the single-lepton control region selection, after normalizing the simulation to data in the control region bins of H_{T}, N_{j}, and N_{b} for events with no b-tagged jets (left), and events with at least one b-tagged jet (right). The hatched bands on the top panels show the MC statistical uncertainty, while the solid gray bands in the ratio plots show the systematic uncertainty in the M_{T2} shape.

one control region is defined for each bin of jet p_{T}. For events with at least two jets, the selected events are binned in H_{T}, N_{j}, and N_{b}, but not in M_{T2}, to increase the dilepton event yield in each control region.

The contribution to each control region from flavor-symmetric processes, most importantly $\mathrm{t\bar{t}}$, is estimated using opposite-flavor (OF) eμ events obtained with the same selections as same-flavor (SF) ee and $\mu\mu$ events. The background in each signal bin is then obtained using transfer factors according to:

$$N^{\mathrm{SR}}_{\mathrm{Z}\to\nu\bar{\nu}}\left(H_{\mathrm{T}}, N_{\mathrm{j}}, N_{\mathrm{b}}, M_{\mathrm{T2}}\right) = \left[N^{\mathrm{CRSF}}_{\ell\ell}\left(H_{\mathrm{T}}, N_{\mathrm{j}}, N_{\mathrm{b}}\right) - N^{\mathrm{CROF}}_{\ell\ell}\left(H_{\mathrm{T}}, N_{\mathrm{j}}, N_{\mathrm{b}}\right) R^{\mathrm{SF/OF}}\right] \times R^{\mathrm{Z}\to\nu\bar{\nu}/\mathrm{Z}\to\ell^+\ell^-}_{\mathrm{MC}}\left(H_{\mathrm{T}}, N_{\mathrm{j}}, N_{\mathrm{b}}\right) k_{\mathrm{Z}\to\nu\bar{\nu}}\left(M_{\mathrm{T2}}\right). \quad (3)$$

Here $N^{\mathrm{CRSF}}_{\ell\ell}$ and $N^{\mathrm{CROF}}_{\ell\ell}$ are the number of SF and OF events in the control region, while $R^{\mathrm{Z}\to\nu\bar{\nu}/\mathrm{Z}\to\ell^+\ell^-}_{\mathrm{MC}}$ and $k_{\mathrm{Z}\to\nu\bar{\nu}}\left(M_{\mathrm{T2}}\right)$ are defined below. The factor $R^{\mathrm{SF/OF}}$ accounts for the difference in acceptance and efficiency between SF and OF events. It is determined as the ratio of the number of SF events to OF events in a $\mathrm{t\bar{t}}$ enriched control sample, obtained with the same selections as the $\mathrm{Z}\to\ell^+\ell^-$ sample, but inverting the requirements on the p_{T} and the invariant mass of the lepton pair. A measured value of $R^{\mathrm{SF/OF}} = 1.07 \pm 0.15$ is observed to be stable with respect to event kinematics, and is applied in all regions. Figure 2 (left) shows $R^{\mathrm{SF/OF}}$ measured as a function of the number of jets.

An estimate of the $\mathrm{Z}\to\nu\bar{\nu}$ background in each topological region is obtained from the corresponding dilepton control region via the factor $R^{\mathrm{Z}\to\nu\bar{\nu}/\mathrm{Z}\to\ell^+\ell^-}_{\mathrm{MC}}$, which accounts for the acceptance and efficiency to select the dilepton pair and the ratio of branching fractions for $\mathrm{Z}\to\ell^+\ell^-$ and $\mathrm{Z}\to\nu\bar{\nu}$ decays. This factor is obtained from simulation, including corrections for differences in the lepton efficiencies between data and simulation.

The factor $k_{\mathrm{Z}\to\nu\bar{\nu}}\left(M_{\mathrm{T2}}\right)$ accounts for the distribution, in bins of M_{T2}, of the estimated back-

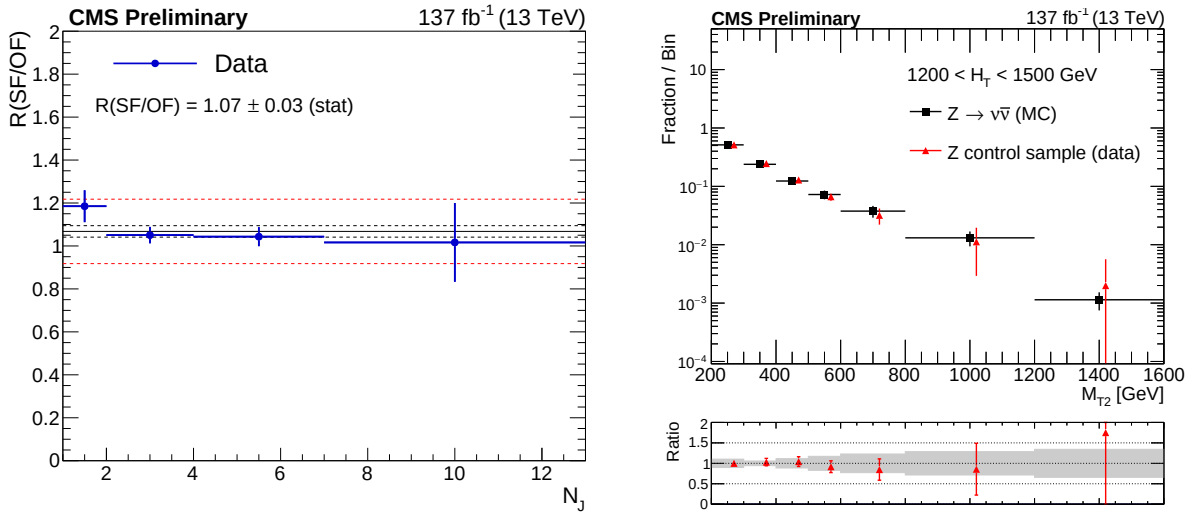

Figure 2: (Left) Ratio $R^{\mathrm{SF/OF}}$ in data as a function of N_{j}. The solid black line enclosed by the red dashed lines corresponds to a value of 1.07 ± 0.15 that is observed to be stable with respect to event kinematics, while the two dashed black lines denote the statistical uncertainty in the $R^{\mathrm{SF/OF}}$ value. (Right) The shape of the M_{T2} distribution in $\mathrm{Z} \to \nu\overline{\nu}$ simulation compared to the one obtained from the $\mathrm{Z} \to \ell^+\ell^-$ data control sample, in a region with $1200 < H_{\mathrm{T}} < 1500\,\mathrm{GeV}$ and $N_{\mathrm{j}} \geq 2$, inclusive in N_{b}. The solid gray band on the ratio plot shows the systematic uncertainty in the M_{T2} shape.

ground in each (H_{T}, N_{j}, N_{b}) topological region. For events with $N_{\mathrm{j}} = 1$, $k_{\mathrm{Z}\to\nu\overline{\nu}}\,(M_{\mathrm{T2}}) = 1$, as no distribution among M_{T2} bins is necessary. For events with $N_{\mathrm{j}} \geq 2$, this distribution is constructed using the M_{T2} shape from dilepton data and $\mathrm{Z} \to \nu\overline{\nu}$ simulation in each topological region. Studies with simulated samples indicate that the M_{T2} shape for $\mathrm{Z} \to \nu\overline{\nu}$ events is independent of N_{b} for a given H_{T} and N_{j} selection, and that the shape is also independent of the number of jets for $H_{\mathrm{T}} > 1500\,\mathrm{GeV}$. The MC modeling of N_{b} and N_{j} as well as of the M_{T2} shape in bins of N_{j} and N_{b} is validated in data, using a dilepton control sample. As a result, M_{T2} templates for topological regions differing only in N_{b} are combined, separately for data and simulation. For $H_{\mathrm{T}} > 1500\,\mathrm{GeV}$, only one M_{T2} template is constructed for data and one for simulation by combining all relevant topological regions.

In each (H_{T}, N_{j}, N_{b}) topological region, an M_{T2} template obtained from dilepton data, corrected by the ratio $R_{\mathrm{MC}}^{\mathrm{Z}\to\nu\overline{\nu}\,/\,\mathrm{Z}\to\ell^+\ell^-}$, is used to distribute the estimated $\mathrm{Z} \to \nu\overline{\nu}$ background in bins of M_{T2}, through the factor $k_{\mathrm{Z}\to\nu\overline{\nu}}\,(M_{\mathrm{T2}})$. At high M_{T2} values, where the dilepton control sample has insufficient statistics, the M_{T2} template is obtained from simulation.

The modeling of M_{T2} is validated in data using control samples enriched in $\mathrm{Z} \to \ell^+\ell^-$ events, in each bin of H_{T}, as shown in the right panel of Fig. 2 for events with $575 < H_{\mathrm{T}} < 1200\,\mathrm{GeV}$.

The largest uncertainty in the estimate of the invisible Z background in most regions results from the limited size of the dilepton control sample. This uncertainty, as well as all other relevant theoretical and experimental uncertainties, are evaluated and propagated to the final estimate. The dominant uncertainty in the ratio $R_{\mathrm{MC}}^{\mathrm{Z}\to\nu\overline{\nu}\,/\,\mathrm{Z}\to\ell^+\ell^-}$ is obtained from measured differences in lepton efficiency between data and simulation, and is about 5%. The uncertainty in the $k_{\mathrm{Z}\to\nu\overline{\nu}}\,(M_{\mathrm{T2}})$ factor arises from data statistics for uncombined bins, while for combined bins it is due to uncertainties in the JES and variations in the renormalization and factorization scales. These can result in effects as large as 40%.

4.1.3 Estimation of the multijet background

The background from multijet events is estimated from control regions in data, selected using triggers that require H_T to exceed thresholds ranging from 125 (180) to 900 (1050) GeV in 2016 (2017–2018). In addition, events are selected with at least one good vertex, and at least two jets with $p_T > 10$ GeV.

The *rebalance and smear* (R&S) method is used to estimate such background, that consists of two steps. In the first step, multijet events are *rebalanced* by adjusting the transverse momenta (p_T) of the jets such that the resulting p_T^{miss} is approximately null. The rebalancing is performed through a likelihood maximization, accounting for the jet energy resolution [55]. The result of the rebalancing step is an inclusive sample of *true* multijet events that are used as a seed for the second step, the *smearing*. In the smearing step, the p_T of the jets in each rebalanced seed event are smeared according to the jet response function, in order to emulate the instrumental effects that lead to non-zero p_T^{miss}. The smearing step is repeated many times for each rebalanced event in order to accumulate statistics in the tails of kinematic distributions such as p_T^{miss} and M_{T2}.

Both the rebalancing and smearing make use of *jet response templates*, which are distributions of the reconstructed jet p_T divided by the generator-level jet p_T. The templates are derived from simulation in bins of jet p_T and η, separately for b-tagged and non-b-tagged jets, and are corrected for differences in the jet energy resolution between data and simulated events.

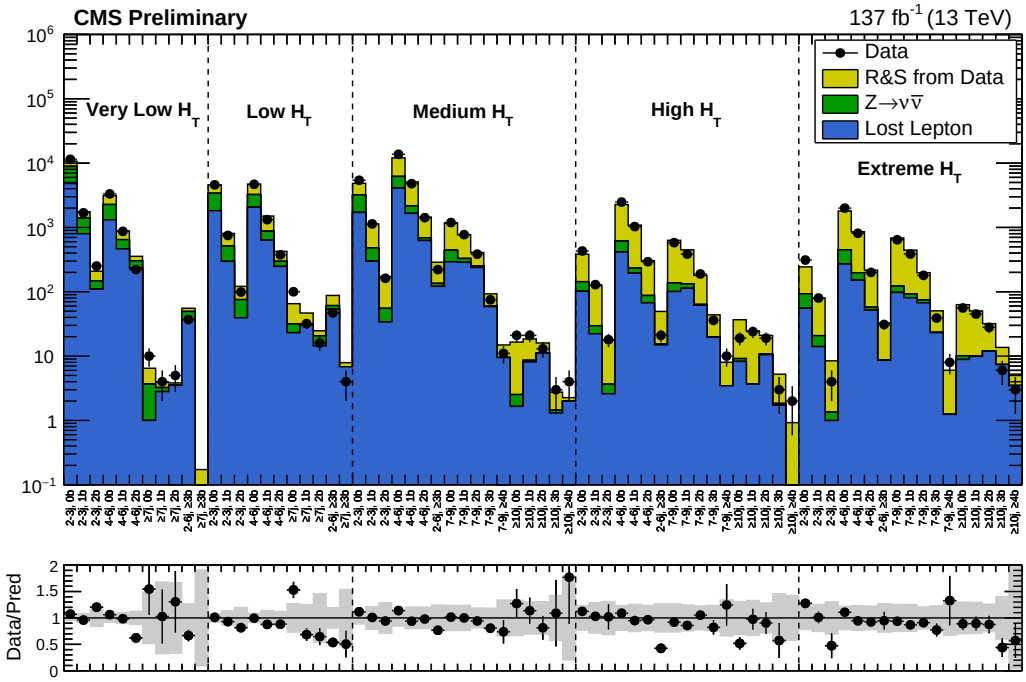

Figure 3: Validation of the R&S multijet background prediction, in control regions in data selected with $\Delta\phi_{min} < 0.3$. Electroweak backgrounds are estimated from data. In regions where statistics in data is insufficient to estimate the electroweak backgrounds, the corresponding yields are taken directly from simulation. Bins on the x-axis are the (H_T, N_{jet}, $N_{b\text{-}jet}$) topological regions. The gray band represents the total uncertainty on the prediction.

Of all jets in the event, a jet *qualifies* to be used, and is used in the rebalancing and smearing procedures if it has $p_T > 10$ GeV, and (if $p_T < 100$ GeV) it is not identified as a jet from pileup. All other jets are left unchanged, but are still used in the calculation of $\vec{p}_T^{miss}$ and other jet-

related quantities. An event with n qualifying jets is rebalanced by varying the $p_{\mathrm{T}}^{\mathrm{reb}}$ of each jet to maximize the likelihood function

$$L = \prod_{i=1}^{n} \mathrm{P}(p_{\mathrm{T},i}^{\mathrm{reco}} | p_{\mathrm{T},i}^{\mathrm{reb}}) \times G\left(\frac{p_{\mathrm{T,reb,x}}^{\mathrm{miss}}}{\sigma_{\mathrm{T}}^{\mathrm{soft}}}\right) \times G\left(\frac{p_{\mathrm{T,reb,y}}^{\mathrm{miss}}}{\sigma_{\mathrm{T}}^{\mathrm{soft}}}\right), \tag{4}$$

where

$$G(x) \equiv e^{-x^2/2} \tag{5}$$

and

$$\vec{p}_{\mathrm{T,reb}}^{\mathrm{miss}} \equiv \vec{p}_{\mathrm{T}}^{\mathrm{miss}} - \sum_{i=1}^{n} \left(\vec{p}_{\mathrm{T},i}^{\mathrm{reb}} - \vec{p}_{\mathrm{T},i}^{\mathrm{reco}}\right). \tag{6}$$

The term $\mathrm{P}(p_{\mathrm{T},i}^{\mathrm{reco}} | p_{\mathrm{T},i}^{\mathrm{reb}})$ in Equation 4 is the probability for a jet with *true* p_{T} of $p_{\mathrm{T},i}^{\mathrm{reb}}$ to be assigned a p_{T} of $p_{\mathrm{T},i}^{\mathrm{reco}}$ after reconstruction. This probability is taken directly from the jet response templates. The two $G(x)$ terms in Equation 4 enforce an approximate balancing condition. The $\vec{p}_{\mathrm{T,reb}}^{\mathrm{miss}}$ terms in Equation 4 represent the missing transverse momentum *after* rebalancing, and are obtained by simply adjusting $\vec{p}_{\mathrm{T}}^{\mathrm{miss}}$ by the changes in jet p_{T} induced by the rebalancing. For the balancing of the x and y components of the missing transverse momentum, a width $\sigma_{\mathrm{T}}^{\mathrm{soft}} = 20$ GeV is used, approximately equal to the width of the x and y components of $\vec{p}_{\mathrm{T}}^{\mathrm{miss}}$ in minimum bias events. This parameter represents the inherent missing energy due to low-p_{T} jets, unclustered energy, and jets from pileup that cannot be eliminated by rebalancing. A systematic uncertainty is assessed to cover for the effects of the variation of $\sigma_{\mathrm{T}}^{\mathrm{soft}}$.

The rebalanced events are used as input to the *smearing* procedure, where the p_{T} of each qualifying jet is rescaled by a random factor drawn from the corresponding jet response template, and all kinematic quantities are recalculated accordingly.

The background from multijet events is estimated from data. In order to remove potential contamination from electroweak sources, events are only used if $p_{T,\mathrm{reb}}^{\mathrm{miss}} < 100\,\mathrm{GeV}$. Such selection is found to be fully efficient for multijet events, in simulation. Hence, no correction is applied to the prediction.

Systematic uncertainties are assessed to cover for the effects listed below, together with the typical size of the associated uncertainty (derived in bins of H_{T}):

- uncertainty on jet energy resolution: 12–19%.
- variation on the size of the tails of the jet response templates: 17–25%.
- variation of $\sigma_{\mathrm{T}}^{\mathrm{soft}}$: 1–12%.
- modeling of N_{j}: 1–21%.
- modeling of N_{b}: 1–25%.

The resulting background prediction is validated in data, in control regions enriched in multijet events. The results of the validation in a control region selected with an inverted requirement on the minimum difference in azimuthal angle between the $\vec{p}_{\mathrm{T}}^{\mathrm{miss}}$ vector and each of the leading four jets, $\Delta\phi_{\mathrm{min}} < 0.3$, orthogonal to the signal region selection, are shown in Figure 3, where also the electroweak background is estimated in data, as described above. In regions where statistics in data is insufficient to estimate the electroweak background, the corresponding yield is taken directly from simulation. The observation is found to agree with the prediction, within uncertainties.

4.2 Search for disappearing tracks

The background from SM processes consists of events containing disappearing tracks from three main sources:

- *fake* tracks.
- charged pions (undergoing a significant interaction in the tracking detector or poorly reconstructed).
- leptons (undergoing a significant interaction in the tracking detector or poorly reconstructed).

The background is estimated from data, leveraging the definition of *short track candidates* (STC) and selected *short tracks* (ST), as follows:

$$N_{\mathrm{ST}}^{est} = f_{\mathrm{short}} \times N_{\mathrm{STC}}^{obs} \,, \tag{7}$$

where N_{ST} is the number of selected *short tracks*, N_{STC} is the number of selected *short track candidates*, and f_{short} is defined as:

$$f_{\mathrm{short}} = N_{\mathrm{ST}}^{obs} \,/\, N_{\mathrm{STC}}^{obs} \,. \tag{8}$$

The f_{short} ratio is measured directly in data, in a control region of events selected using the same triggers and preselections used for the signal regions, except the selection on $p_{\mathrm{T}}^{\mathrm{miss}}$ is relaxed to $p_{\mathrm{T}}^{\mathrm{miss}} > 30\,\mathrm{GeV}$ for any H_{T}, and the selection on M_{T2} is shifted to $60 < M_{\mathrm{T2}} < 100\,\mathrm{GeV}$. We exploit the empirical invariance of this ratio with respect to H_{T} and $p_{\mathrm{T}}^{\mathrm{miss}}$ selections, in order to reduce the statistical uncertainty on its measurement. The f_{short} ratio is therefore measured in data separately for each N_{j}, track p_{T}, track length category, and inclusively in H_{T} (with $H_{\mathrm{T}} > 250\,\mathrm{GeV}$). The f_{short} values are measured separately in 2016 data and 2017–2018 data, mainly to account for the upgrade of the CMS tracking detector after 2016. Since a reliable measurement in data of the f_{short} ratio for long (L) tracks is not achievable, due to the insufficient statistics, the value measured in data for medium length (M) tracks is used, after a correction based on simulation:

$$f_{\mathrm{short}}(L)_{\mathrm{Data}}^{est} = f_{\mathrm{short}}(M)_{\mathrm{Data}} \times f_{\mathrm{short}}(L)_{\mathrm{MC}} / f_{\mathrm{short}}(M)_{\mathrm{MC}} \,. \tag{9}$$

A systematic uncertainty on the measured values of f_{short} is assessed, in order to cover for the empirically motivated assumption of invariance with respect to H_{T} and $p_{\mathrm{T}}^{\mathrm{miss}}$. Its size is determined by varying such selection requirements in events with $60 < M_{\mathrm{T2}} < 100\,\mathrm{GeV}$, in data. For long (L) tracks, a systematic uncertainty of 100% is assessed, as a correction based on simulation is used and there are insufficient statistics to study the effect of H_{T} and $p_{\mathrm{T}}^{\mathrm{miss}}$ variations.

The f_{short} ratio is then used to predict the expected background in events with $M_{\mathrm{T2}} > 100\,\mathrm{GeV}$, as described in Equation 7.

The background prediction is validated in data in an intermediate M_{T2} validation region ($100 < M_{\mathrm{T2}} < 200\,\mathrm{GeV}$), orthogonal to the high M_{T2} signal region ($M_{\mathrm{T2}} > 200\,\mathrm{GeV}$). Event categorization in the validation region (VR) is identical to the signal region. Hence, it is possible to validate the background prediction in each search bin separately.

Figure 4 shows the result of the background prediction validation in 2016 data and in 2017–2018 data. We find good agreement between the observation and the background prediction in the validation region. An additional systematic uncertainty is assessed in order to cover for discrepancies exceeding statistical uncertainties.

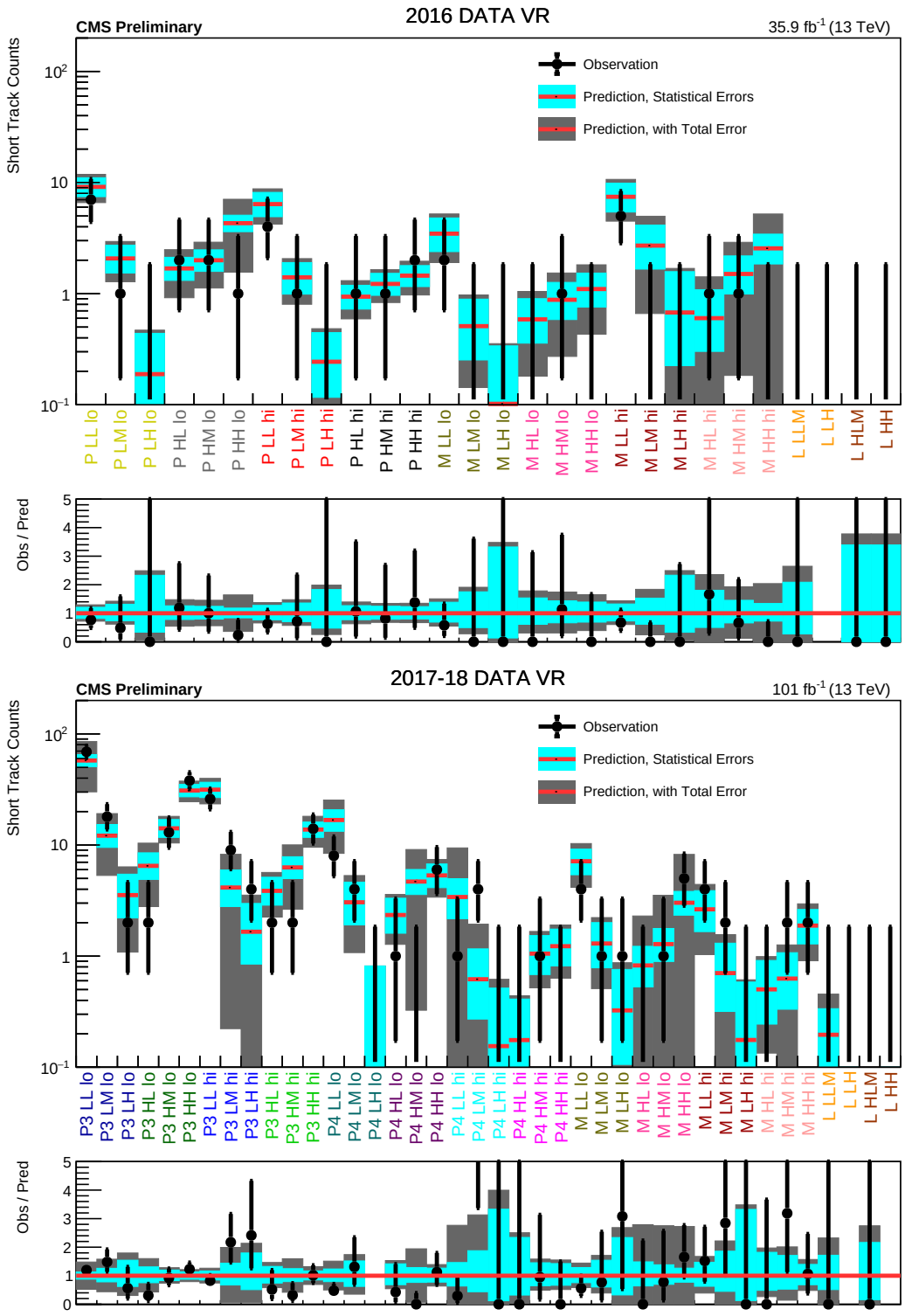

Figure 4: Validation of the background prediction method in (upper) the 2016 data validation region, and in (lower) the 2017–2018 data validation region, in the search for disappearing tracks. The red histogram represents the predicted background, while the black points are the actual observed data counts. The cyan band represents the statistical uncertainty on the prediction. The gray band represents the total uncertainty. The labels on the x-axes are explained in Tables 7–8 of Appendix B.2. Regions whose predictions use the same measurement of f_{short} are identified by the colors of the labels. Bins with no entry in the ratio have zero predicted background.

5 Results

The data yields in the search regions are statistically compatible with the estimated backgrounds from SM processes.

5.1 Inclusive M_{T2} search

A summary of the results of the M_{T2} inclusive search is shown in Fig. 5. Each bin in Fig. 5 (upper) corresponds to a single (H_{T}, N_{j}, N_{b}) topological region, integrated over M_{T2}. Figure 5 (lower) further breaks down the background estimates and observed data yields into M_{T2} bins for the region $575 < H_{\mathrm{T}} < 1200\,\mathrm{GeV}$: each bin corresponds to a single M_{T2} bin, and vertical lines identify (H_{T}, N_{j}, N_{b}) topological regions. Distributions for the other H_{T} regions can be found in Appendix C.1. The background estimates and corresponding uncertainties shown in these plots rely exclusively on the inputs from control samples and simulation described in Section 4.1, and are referred to in the rest of the text as *pre-fit background* results.

5.2 Search for disappearing tracks

The results of the search for disappearing tracks are shown in Fig. 6. The background estimates and corresponding uncertainties shown in these plots rely exclusively on the inputs from control samples and simulation described in Section 4.2, and are referred to in the rest of the text as *pre-fit background* results.

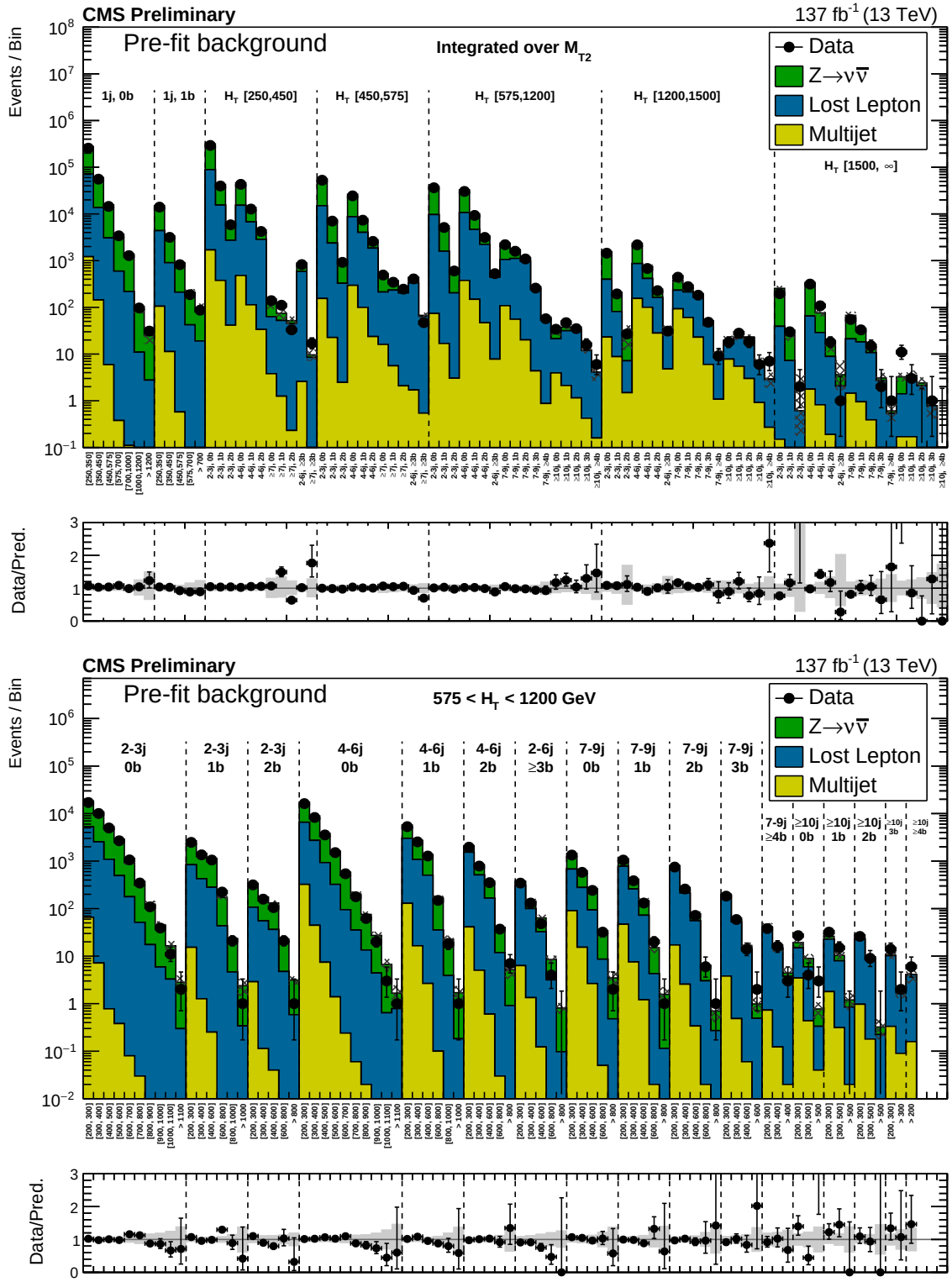

Figure 5: (Upper) Comparison of estimated (pre-fit) background and observed data events in each topological region. Hatched bands represent the full uncertainty in the background estimate. The monojet regions ($N_j = 1$) are identified by the labels "1j, 0b" and "1j, 1b", and are binned in jet p_T. The multijet ones are shown for each H_T region separately, and are labeled accordingly. The notations j, b indicate N_j, N_b labeling. (Lower) Same for individual M_{T2} signal bins in the medium H_T region. On the x-axis, the M_{T2} binning is shown in units of GeV.

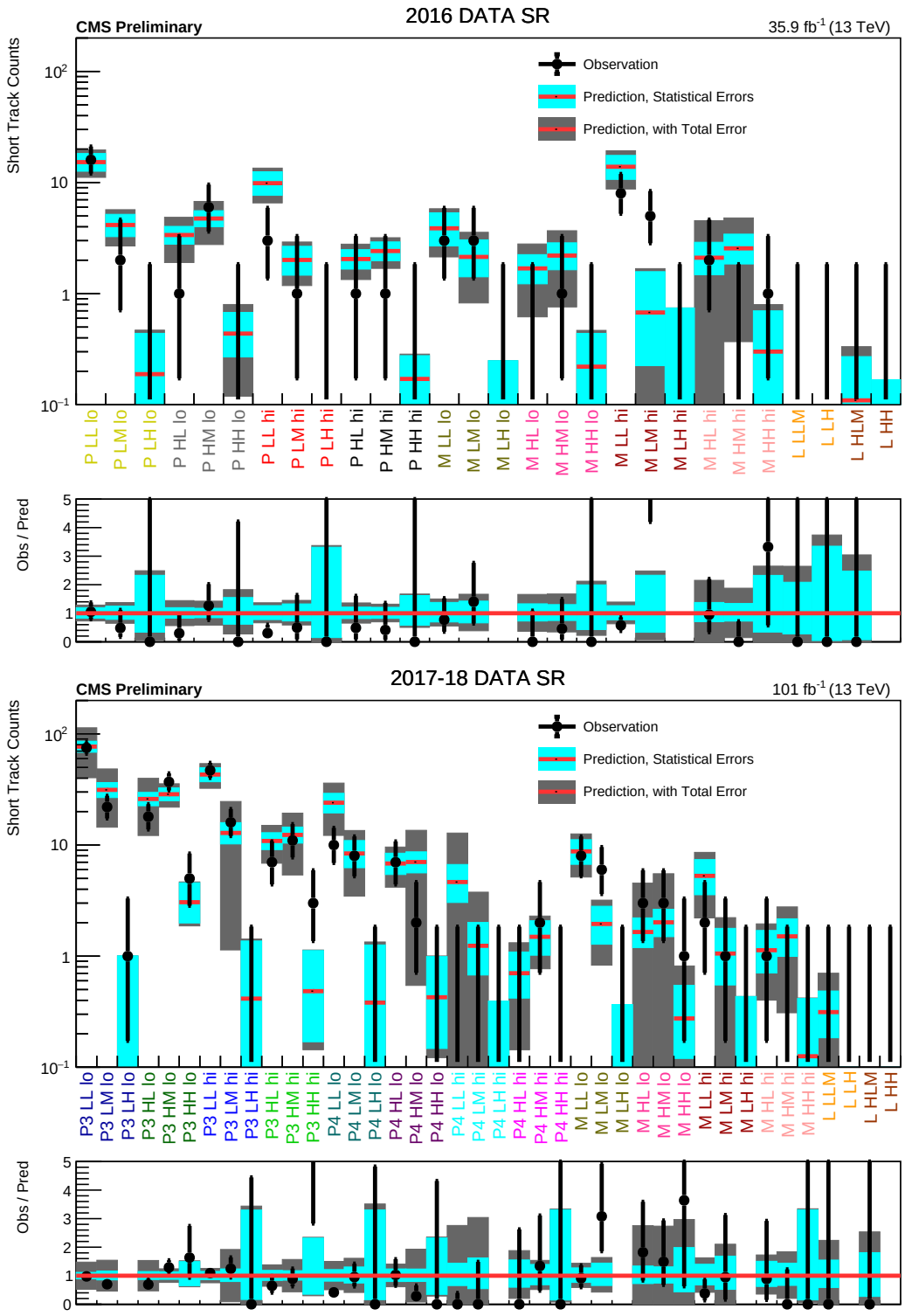

Figure 6: Comparison of estimated (pre-fit) background and observed data events in (upper) each of the 2016 search regions, and in (lower) each of the 2017–2018 search regions, in the search for disappearing tracks. The red histogram represents the predicted background, while the black points are the actual observed data counts. The cyan band represents the statistical uncertainty on the prediction. The gray band represents the total uncertainty. The labels on the x-axes are explained in Tables 7–8 of Appendix B.2. Regions whose predictions use the same measurement of f_{short} are identified by the colors of the labels. Bins with no entry in the ratio have zero (pre-fit) predicted background.

6 Interpretation

The results of the searches can be interpreted by performing a maximum likelihood fit to the data in the signal regions. The fit is carried out under either a background-only or a background+signal hypothesis. The uncertainties in the modeling of the backgrounds, summarized in Section 4, are inputs to the fitting procedure. The likelihood is constructed as the product of Poisson probability density functions, one for each signal region, with additional log-normal constraint terms that account for uncertainties in the background estimates and, if considered, the signal yields. The result of the background-only fit is denoted as *post-fit background*, and is given in Appendix C.2 for the inclusive M_{T2} search, and in Appendix C.3 for the search for disappearing tracks. If the uncertainties associated to the pre-fit estimates are properly sized, the assumed correlation model across signal regions is correct, and the data are found to be in agreement with the estimates, then the fit has the effect of constraining the background and reducing the associated uncertainties.

The results of the inclusive M_{T2} search are used to constrain the simplified models of SUSY [56] shown in Fig. 7. For each scenario of gluino (squark) pair production, the simplified models assume that all SUSY particles other than the gluino (squark) and the lightest neutralino are too heavy to be produced directly, and that the gluino (squark) decays promptly. The models assume that each gluino (squark) decays with a 100% branching fraction into the decay products depicted in Fig. 7. For the scenario of top squark pair production, the polarization of the top quark is model dependent and is a function of the top-squark and neutralino mixing matrices. To remain agnostic to a particular model realization, events are generated without polarization. Signal cross sections are calculated at approximate-NNLO+NNLL order in α_{s} [57–62].

The results of the search for disappearing tracks are used to constrain analogous simplified models of SUSY, where gluinos are pair-produced, and each decays either directly to the lightest neutralino ($\widetilde{\chi}_1^0$), or first to a long-lived chargino ($\widetilde{\chi}_1^{\pm}$) as shown in Fig. 8. Each possible decay is taken to occur with equal probability. Thus, the gluino branching fraction is $\frac{1}{3}$ each, for the decay to $\widetilde{\chi}_1^0$, $\widetilde{\chi}_1^+$ and $\widetilde{\chi}_1^-$. The masses of the $\widetilde{\chi}_1^{\pm}$ and of the $\widetilde{\chi}_1^0$ are assumed to differ by a few hundred MeV [16, 17]. The $\widetilde{\chi}_1^{\pm}$ decays to a $\widetilde{\chi}_1^0$ and a charged pion, with a limited phase space. As a consequence, the $\widetilde{\chi}_1^{\pm}$ has a short lifetime (a few ns), and the momentum of the pion originating from its decay does not exceed a few hundred MeV. Hence, the final state shows negligible dependence on small variations of the mass difference between $\widetilde{\chi}_1^{\pm}$ and $\widetilde{\chi}_1^0$.

Typical values of the uncertainties in the signal yield for the simplified models considered are listed in Table 2. The sources of uncertainties and the methods used to evaluate their effect on the interpretation are the same as those discussed in Refs. [2, 3]. For each year (2016, 2017, and 2018), uncertainties due to the luminosity [63, 64] , ISR, fast simulation $p_{\mathrm{T}}^{\mathrm{miss}}$, and b tagging and lepton efficiencies are treated as correlated across search bins. Uncertainties on fast simulation $p_{\mathrm{T}}^{\mathrm{miss}}$, b tagging and lepton efficiencies are treated as correlated also across years. Remaining uncertainties are taken as uncorrelated. In the search for disappearing tracks, uncertainties on b tagging and lepton efficiencies are not considered. On the other hand, additional uncertainties are assessed to account for the modeling of disappearing tracks, and are treated as correlated across search bins. Specifically, an uncertainty of 10% in the signal yield is assigned, equal to one half of the track selection inefficiency, together with an uncertainty of 6%, equal to one half of the difference in acceptance due to the use of fast simuation.

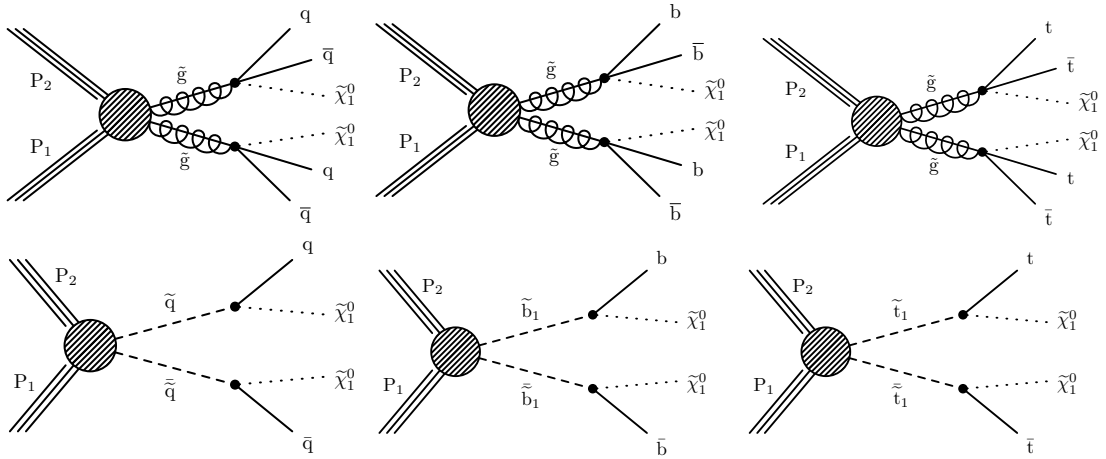

Figure 7: (Upper) Diagrams for the three scenarios of gluino-mediated light-flavor squark, bottom squark and top squark production considered. (Lower) Diagrams for the direct production of light-flavor, bottom and top squark pairs.

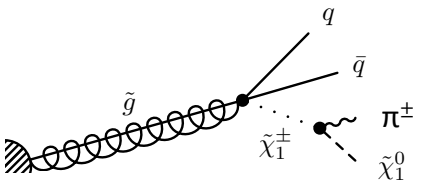

Figure 8: Diagram showing the decays of a gluino via a long-lived $\tilde{\chi}_1^{\pm}$. The mass of the $\tilde{\chi}_1^{\pm}$ is larger than the mass of the $\tilde{\chi}_1^0$ by few hundred MeV. The $\tilde{\chi}_1^{\pm}$ decays to a $\tilde{\chi}_1^0$ via a pion, too soft to be detected.

Table 2: Typical values of the systematic uncertainties as evaluated for the simplified models of SUSY used in the context of this search. The high statistical uncertainty in the simulated signal sample corresponds to a small number of signal bins with low acceptance, which are typically not among the most sensitive signal bins to that model point.

Source	Range [%]
Integrated luminosity	2.3–2.5
Limited size of MC samples	1–100
Renormalization and factorization scales	5
ISR modeling	0–30
b tagging efficiency, heavy flavors	0–40
b tagging efficiency, light flavors	0–20
Lepton efficiency	0–20
Jet energy scale	5
Fast simulation $p_{\mathrm{T}}^{\mathrm{miss}}$ modeling	0–5

6.1 Inclusive M_{T2} search

Figure 9 shows the exclusion limits at 95% CL for gluino-mediated bottom squark, top squark, and light-flavor squark production. Exclusion limits at 95% CL for the direct production of bottom, top, and light-flavor squark pairs are shown in Fig. 10.

These results extend the constraints on gluinos and squarks by about 100–350 GeV and on $\widetilde{\chi}_1^0$ by 100–250 GeV with respect to those in Ref. [2].

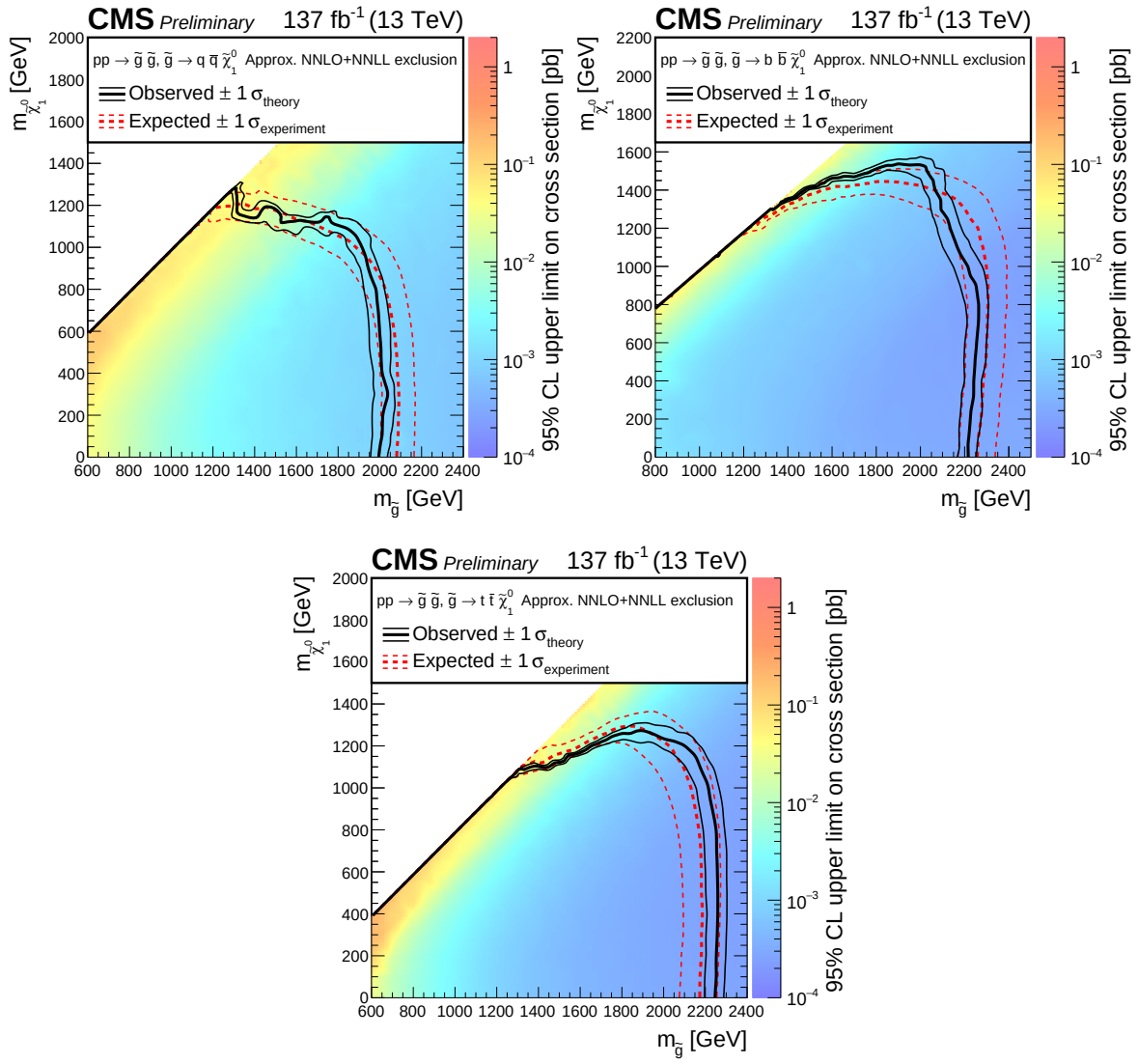

Figure 9: Exclusion limits at 95% CL for gluino-mediated light-flavor (u,d,s,c) squark production (above left), gluino-mediated bottom squark production (above right), and gluino-mediated top squark production (below). The area enclosed by the thick black curve represents the observed exclusion region, while the dashed red lines indicate the expected limits and their ± 1 standard deviation ranges. The thin black lines show the effect of the theoretical uncertainties on the signal cross section.

6.2 Search for disappearing tracks

Figure 11 shows the exclusion limits at 95% CL for gluino-mediated light-flavor squark production, with $c\tau_0(\tilde{\chi}_1^{\pm}) = 10$, 50, and 200 cm.

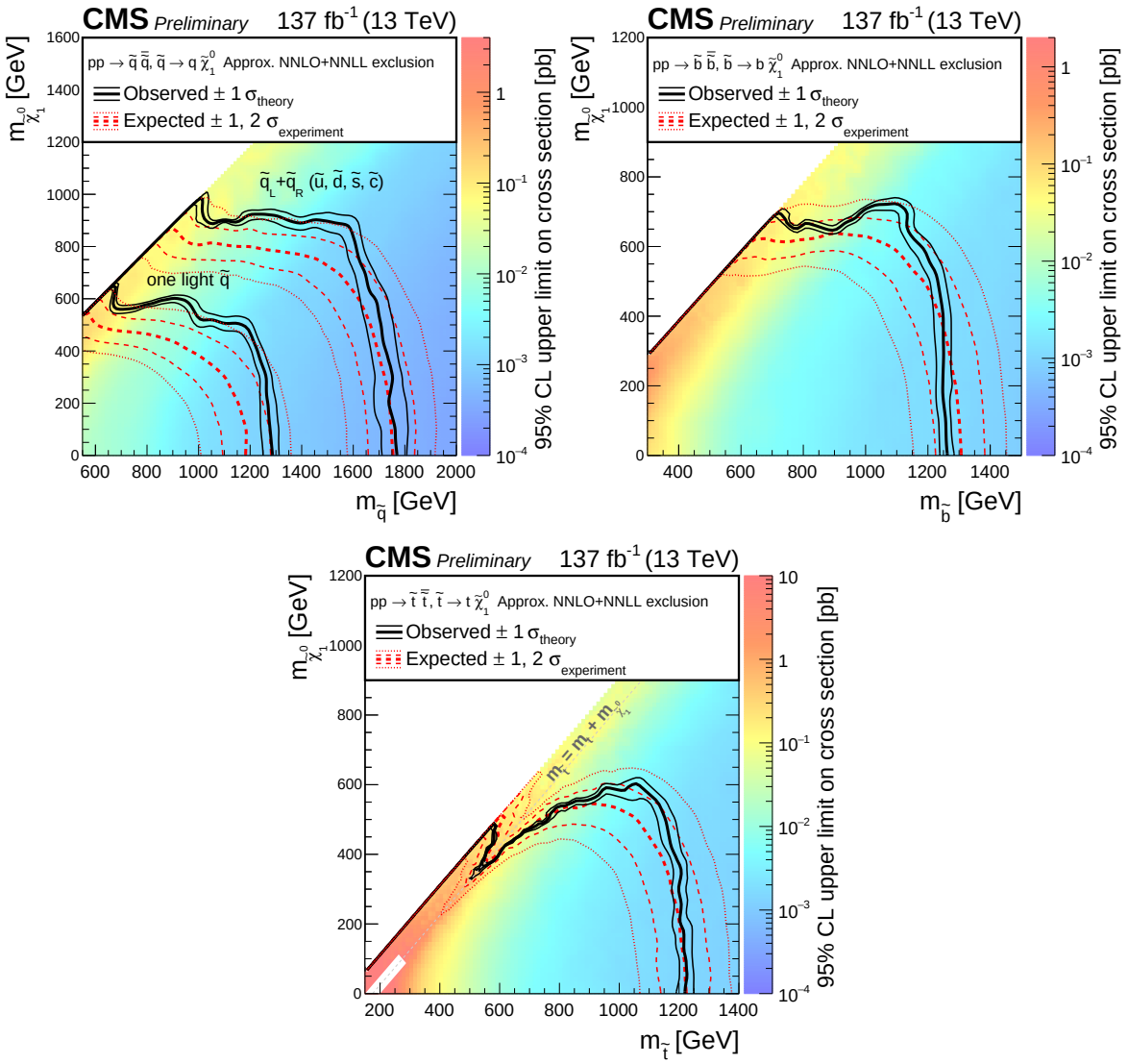

Figure 10: Exclusion limit at 95% CL for light-flavor squark pair production (above left), bottom squark pair production (above right), and top squark pair production (below). The area enclosed by the thick black curve represents the observed exclusion region, while the dashed red lines indicate the expected limits and their ± 1 and ± 2 standard deviation ranges. The thin black lines show the effect of the theoretical uncertainties on the signal cross section. The white diagonal band in the top squark pair production exclusion limit corresponds to the region $|m_{\tilde{t}} - m_t - m_{\tilde{\chi}_1^0}| < 25\,\text{GeV}$ and small $m_{\tilde{\chi}_1^0}$. Here the efficiency of the selection is a strong function of $m_{\tilde{t}} - m_{\tilde{\chi}_1^0}$, and as a result the precise determination of the cross section upper limit is uncertain because of the finite granularity of the available MC samples in this region of the $(m_{\tilde{t}}, m_{\tilde{\chi}_1^0})$ plane.

Exclusion limits from the disappearing track search tend to be strongest in longer $c\tau_0(\tilde{\chi}_1^\pm)$ models when $m_{\tilde{\chi}_1^0}$ is near the mass of the gluino, and in shorter $c\tau_0(\tilde{\chi}_1^\pm)$ models when a large mass splitting generates a large boost for the $\tilde{\chi}_1^\pm$. In the massless $\tilde{\chi}_1^\pm$ and $\widetilde{\chi}_1^0$ limit, the $\tilde{\chi}_1^\pm$ receives a large boost and so does not typically decay inside the tracking detector, reducing signal acceptance and analysis sensitivity.

When a $\tilde{\chi}_1^\pm$ decays within the volume of the tracking detector, it is not counted as a particle-flow candidate, and being almost mass degenerate with the $\widetilde{\chi}_1^0$, its decay products provide negligible visible energy in the detector. As a result, the limits presented in Sec. 6.1 from the inclusive M_{T2} search should apply also to these models with an intermediate $\tilde{\chi}_1^\pm$, to good approximation. As shown in Fig. 11, the search for disappearing tracks significantly extends the sensitivity of the inclusive M_{T2} search.

7 Summary

This note presents the results of two related searches for new phenomena using events with jets and large M_{T2}. Results are based on a 137 fb^{-1} data sample of proton-proton collisions at $\sqrt{s} = 13\,\mathrm{TeV}$ collected in 2016, 2017 and 2018 with the CMS detector. No significant deviations from the standard model expectations are observed. The results are interpreted as limits on pair-produced gluinos and squarks in simplified models of R-parity conserving supersymmetry. The inclusive M_{T2} search probes gluino masses up to 2250 GeV and $\widetilde{\chi}_1^0$ masses up to 1525 GeV, as well as light-flavor, bottom, and top squark masses up to 1770, 1260, and 1225 GeV, respectively, and $\widetilde{\chi}_1^0$ masses up to 975, 725, and 600 GeV in each scenario. The search for disappearing tracks extends the gluino mass limit to as much as 2460 GeV, and the $\widetilde{\chi}_1^0$ mass limit to as much as 2000 GeV, in models where the gluino can decay with equal probability to $\widetilde{\chi}_1^0$, $\tilde{\chi}_1^+$, and $\tilde{\chi}_1^-$, and the $\tilde{\chi}_1^\pm$ are long-lived.

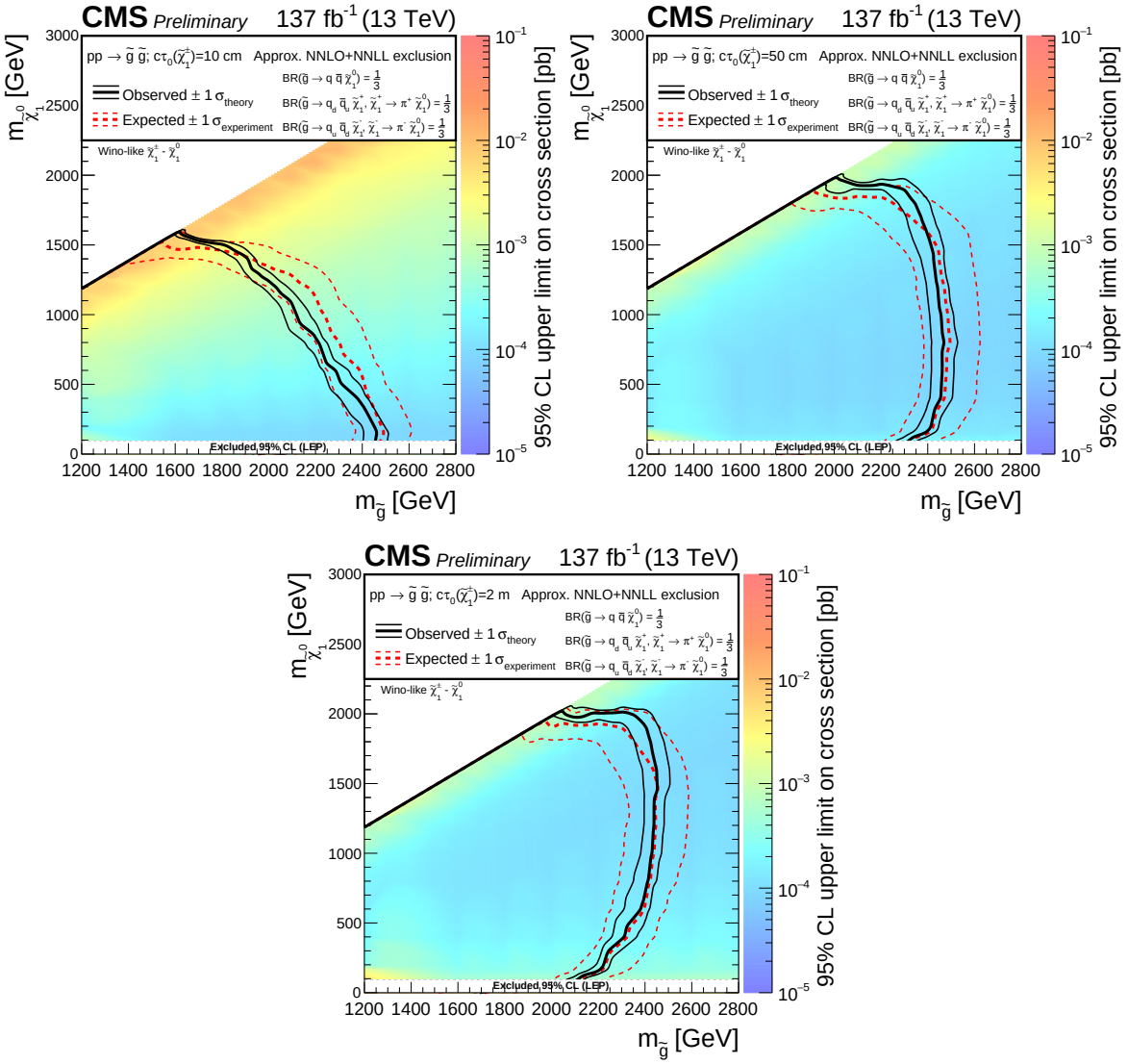

Figure 11: Exclusion limits at 95% CL for gluino-mediated light-flavor (u,d,s,c) squark production with $c\tau_0(\tilde{\chi}_1^{\pm}) = 10$ cm (above left), 50 cm (above right), and 200 cm (below). The area enclosed by the thick black curve represents the observed exclusion region, while the dashed red lines indicate the expected limits and their ± 1 standard deviation ranges. The thin black lines show the effect of the theoretical uncertainties on the signal cross section. The white band for masses of the $\tilde{\chi}_1^0$ below 91.9 GeV represent the region of the mass plane excluded at LEP [65].

References

[1] C. G. Lester and D. J. Summers, "Measuring masses of semiinvisibly decaying particles pair produced at hadron colliders", *Phys. Lett. B* **463** (1999) 99, doi:10.1016/S0370-2693(99)00945-4, arXiv:hep-ph/9906349.

[2] CMS Collaboration, "Search for new phenomena with the M_{T2} variable in the all-hadronic final state produced in proton-proton collisions at $\sqrt{s} = 13$ TeV", *Eur. Phys. J.* **C77** (2017), no. 10, 710, doi:10.1140/epjc/s10052-017-5267-x, arXiv:1705.04650.

[3] CMS Collaboration, "Search for new physics with the M_{T2} variable in all-jets final states produced in pp collisions at $\sqrt{s} = 13$ TeV", *JHEP* **10** (2016) 006, doi:10.1007/JHEP10(2016)006, arXiv:1603.04053.

[4] CMS Collaboration, "Searches for supersymmetry using the m_{T2} variable in hadronic events produced in pp collisions at 8 tev", *JHEP* **05** (2015) 078, doi:10.1007/JHEP05(2015)078, arXiv:1502.04358.

[5] CMS Collaboration, "Search for supersymmetry in hadronic final states using M_{T2} in pp collisions at $\sqrt{s} = 7$ TeV", *JHEP* **10** (2012) 018, doi:10.1007/JHEP10(2012)018, arXiv:1207.1798.

[6] ATLAS Collaboration, "Search for squarks and gluinos in final states with jets and missing transverse momentum using 36 fb^{-1} of $\sqrt{s} = 13$ TeV pp collision data with the ATLAS detector", *Phys. Rev.* **D97** (2018), no. 11, 112001, doi:10.1103/PhysRevD.97.112001, arXiv:1712.02332.

[7] ATLAS Collaboration, "Search for new phenomena with large jet multiplicities and missing transverse momentum using large-radius jets and flavour-tagging at ATLAS in 13 TeV pp collisions", *JHEP* **12** (2017) 034, doi:10.1007/JHEP12(2017)034, arXiv:1708.02794.

[8] ATLAS Collaboration, "Search for dark matter and other new phenomena in events with an energetic jet and large missing transverse momentum using the ATLAS detector", *JHEP* **01** (2018) 126, doi:10.1007/JHEP01(2018)126, arXiv:1711.03301.

[9] ATLAS Collaboration, "Search for supersymmetry in final states with missing transverse momentum and multiple b-jets in proton-proton collisions at $\sqrt{s} = 13$ TeV with the ATLAS detector", *JHEP* **06** (2018) 107, doi:10.1007/JHEP06(2018)107, arXiv:1711.01901.

[10] ATLAS Collaboration, "Search for a scalar partner of the top quark in the jets plus missing transverse momentum final state at $\sqrt{s}$=13 TeV with the ATLAS detector", *JHEP* **12** (2017) 085, doi:10.1007/JHEP12(2017)085, arXiv:1709.04183.

[11] ATLAS Collaboration, "Search for supersymmetry in events with b-tagged jets and missing transverse momentum in pp collisions at $\sqrt{s} = 13$ TeV with the ATLAS detector", *JHEP* **11** (2017) 195, doi:10.1007/JHEP11(2017)195, arXiv:1708.09266.

[12] CMS Collaboration, "Constraints on models of scalar and vector leptoquarks decaying to a quark and a neutrino at $\sqrt{s} = 13$ TeV", *Phys. Rev.* **D98** (2018), no. 3, 032005, doi:10.1103/PhysRevD.98.032005, arXiv:1805.10228.

[13] CMS Collaboration, "Search for supersymmetry in multijet events with missing transverse momentum in proton-proton collisions at 13 TeV", *Phys. Rev.* **D96** (2017), no. 3, 032003, doi:10.1103/PhysRevD.96.032003, arXiv:1704.07781.

[14] CMS Collaboration, "Search for natural and split supersymmetry in proton-proton collisions at $\sqrt{s} = 13$ TeV in final states with jets and missing transverse momentum", *JHEP* **05** (2018) 025, doi:10.1007/JHEP05(2018)025, arXiv:1802.02110.

[15] CMS Collaboration, "Inclusive search for supersymmetry in pp collisions at $\sqrt{s} = 13$ TeV using razor variables and boosted object identification in zero and one lepton final states", (2018). arXiv:1812.06302. Submitted to: *JHEP*.

[16] G. F. Giudice, M. A. Luty, H. Murayama, and R. Rattazzi, "Gaugino mass without singlets", *JHEP* **12** (1998) 027, doi:10.1088/1126-6708/1998/12/027, arXiv:hep-ph/9810442.

[17] L. Randall and R. Sundrum, "Out of this world supersymmetry breaking", *Nucl. Phys.* **B557** (1999) 79–118, doi:10.1016/S0550-3213(99)00359-4, arXiv:hep-th/9810155.

[18] ATLAS Collaboration, "Search for long-lived charginos based on a disappearing-track signature in pp collisions at $\sqrt{s} = 13$ TeV with the ATLAS detector", *JHEP* **06** (2018) 022, doi:10.1007/JHEP06(2018)022, arXiv:1712.02118.

[19] CMS Collaboration, "Search for disappearing tracks as a signature of new long-lived particles in proton-proton collisions at $\sqrt{s} = 13$ TeV", *JHEP* **08** (2018) 016, doi:10.1007/JHEP08(2018)016, arXiv:1804.07321.

[20] CMS Collaboration, "Search for long-lived charged particles in proton-proton collisions at $\sqrt{s} = 13$ TeV", *Phys. Rev.* **D94** (2016), no. 11, 112004, doi:10.1103/PhysRevD.94.112004, arXiv:1609.08382.

[21] CMS Collaboration, "Constraints on the pMSSM, AMSB model and on other models from the search for long-lived charged particles in proton-proton collisions at sqrt(s) = 8 TeV", *Eur. Phys. J.* **C75** (2015), no. 7, 325, doi:10.1140/epjc/s10052-015-3533-3, arXiv:1502.02522.

[22] P. Ramond, "Dual theory for free fermions", *Phys. Rev. D* **3** (1971) 2415, doi:10.1103/PhysRevD.3.2415.

[23] Y. A. Gol'fand and E. P. Likhtman, "Extension of the algebra of Poincaré group generators and violation of P invariance", *JETP Lett.* **13** (1971) 323.

[24] A. Neveu and J. H. Schwarz, "Factorizable dual model of pions", *Nucl. Phys. B* **31** (1971) 86, doi:10.1016/0550-3213(71)90448-2.

[25] D. V. Volkov and V. P. Akulov, "Possible universal neutrino interaction", *JETP Lett.* **16** (1972) 438.

[26] J. Wess and B. Zumino, "A lagrangian model invariant under supergauge transformations", *Phys. Lett. B* **49** (1974) 52, doi:10.1016/0370-2693(74)90578-4.

[27] J. Wess and B. Zumino, "Supergauge transformations in four dimensions", *Nucl. Phys. B* **70** (1974) 39, doi:10.1016/0550-3213(74)90355-1.

[28] P. Fayet, "Supergauge invariant extension of the Higgs mechanism and a model for the electron and its neutrino", *Nucl. Phys. B* **90** (1975) 104, doi:10.1016/0550-3213(75)90636-7.

[29] H. P. Nilles, "Supersymmetry, supergravity and particle physics", *Phys. Rep.* **110** (1984) 1, doi:10.1016/0370-1573(84)90008-5.

[30] CMS Collaboration, "The CMS experiment at the CERN LHC", *JINST* **3** (2008) S08004, doi:10.1088/1748-0221/3/08/S08004.

[31] CMS Collaboration, "The CMS trigger system", *JINST* **12** (2017), no. 01, P01020, doi:10.1088/1748-0221/12/01/P01020, arXiv:1609.02366.

[32] CMS Collaboration, "Particle-flow reconstruction and global event description with the CMS detector", *JINST* **12** (2017), no. 10, P10003, doi:10.1088/1748-0221/12/10/P10003, arXiv:1706.04965.

[33] M. Cacciari, G. P. Salam, and G. Soyez, "The anti-k_t jet clustering algorithm", *JHEP* **04** (2008) 063, doi:10.1088/1126-6708/2008/04/063, arXiv:0802.1189.

[34] M. Cacciari, G. P. Salam, and G. Soyez, "FastJet user manual", *Eur. Phys. J. C* **72** (2012) 1896, doi:10.1140/epjc/s10052-012-1896-2, arXiv:1111.6097.

[35] M. Cacciari and G. P. Salam, "Pileup subtraction using jet areas", *Phys. Lett. B* **659** (2008) 119, doi:10.1016/j.physletb.2007.09.077, arXiv:0707.1378.

[36] CMS Collaboration, "Identification of heavy-flavour jets with the CMS detector in pp collisions at 13 TeV", *JINST* **13** (2018), no. 05, P05011, doi:10.1088/1748-0221/13/05/P05011, arXiv:1712.07158.

[37] CMS Collaboration, "Missing transverse energy performance of the CMS detector", *JINST* **6** (2011) P09001, doi:10.1088/1748-0221/6/09/P09001, arXiv:1106.5048.

[38] CMS Collaboration, "Performance of missing transverse momentum in pp collisions at sqrt(s)=13 TeV using the CMS detector", Technical Report CMS-PAS-JME-17-001, CERN, Geneva, 2018.

[39] T. Sjöstrand, "The Lund Monte Carlo for e^+e^- jet physics", *Comput. Phys. Commun.* **28** (1983) 229, doi:10.1016/0010-4655(83)90041-3.

[40] T. Sjöstrand, S. Mrenna, and P. Skands, "PYTHIA 6.4 physics and manual", *JHEP* **05** (2006) 026, doi:10.1088/1126-6708/2006/05/026, arXiv:hep-ph/0603175.

[41] UA1 Collaboration, "Experimental Observation of Isolated Large Transverse Energy Electrons with Associated Missing Energy at s**(1/2) = 540-GeV", *Phys. Lett.* **B122** (1983) 103–116, doi:10.1016/0370-2693(83)91177-2. [,611(1983)].

[42] J. Alwall et al., "The automated computation of tree-level and next-to-leading order differential cross sections, and their matching to parton shower simulations", *JHEP* **07** (2014) 079, doi:10.1007/JHEP07(2014)079, arXiv:1405.0301.

[43] J. Alwall et al., "Comparative study of various algorithms for the merging of parton showers and matrix elements in hadronic collisions", *Eur. Phys. J. C* **53** (2008) 473, doi:10.1140/epjc/s10052-007-0490-5, arXiv:0706.2569.

[44] T. Sjöstrand, S. Mrenna, and P. Skands, "A brief introduction to PYTHIA 8.1", *Comp. Phys. Comm.* **178** (2008) 852, doi:10.1016/j.cpc.2008.01.036, arXiv:0710.3820.

[45] S. Alioli, P. Nason, C. Oleari, and E. Re, "NLO single-top production matched with shower in POWHEG: s- and t-channel contributions", *JHEP* **09** (2009) 111, doi:10.1088/1126-6708/2009/09/111, arXiv:0907.4076. [Erratum: doi:10.1007/JHEP02(2010)011].

[46] E. Re, "Single-top Wt-channel production matched with parton showers using the POWHEG method", *Eur. Phys. J. C* **71** (2011) 1547, doi:10.1140/epjc/s10052-011-1547-z, arXiv:1009.2450.

[47] GEANT4 Collaboration, "GEANT4—a simulation toolkit", *Nucl. Instrum. Meth. A* **506** (2003) 250, doi:10.1016/S0168-9002(03)01368-8.

[48] S. Abdullin et al., "The fast simulation of the CMS detector at LHC", *J. Phys. Conf. Ser.* **331** (2011) 032049, doi:10.1088/1742-6596/331/3/032049.

[49] R. Gavin, Y. Li, F. Petriello, and S. Quackenbush, "FEWZ 2.0: A code for hadronic Z production at next-to-next-to-leading order", *Comput. Phys. Commun.* **182** (2011) 2388, doi:10.1016/j.cpc.2011.06.008, arXiv:1011.3540.

[50] R. Gavin, Y. Li, F. Petriello, and S. Quackenbush, "W physics at the LHC with FEWZ 2.1", *Comput. Phys. Commun.* **184** (2013) 208, doi:10.1016/j.cpc.2012.09.005, arXiv:1201.5896.

[51] M. Czakon and A. Mitov, "Top++: A program for the calculation of the top-pair cross-section at hadron colliders", *Comput. Phys. Commun.* **185** (2014) 2930, doi:10.1016/j.cpc.2014.06.021, arXiv:1112.5675.

[52] J. Alwall et al., "The automated computation of tree-level and next-to-leading order differential cross sections, and their matching to parton shower simulations", *JHEP* **07** (2014) 079, doi:10.1007/JHEP07(2014)079, arXiv:1405.0301.

[53] C. Borschensky et al., "Squark and gluino production cross sections in pp collisions at $\sqrt{s} = 13$, 14, 33 and 100 TeV", *Eur. Phys. J. C* **74** (2014) 3174, doi:10.1140/epjc/s10052-014-3174-y, arXiv:1407.5066.

[54] CMS Collaboration, "Measurements of $t\bar{t}$ cross sections in association with b jets and inclusive jets and their ratio using dilepton final states in pp collisions at $\sqrt{s} = 13$ TeV", *Phys. Lett.* **B776** (2018) 355–378, doi:10.1016/j.physletb.2017.11.043, arXiv:1705.10141.

[55] CMS Collaboration, "Jet energy scale and resolution performance with 13 TeV data collected by CMS in 2016", Technical Report CMS-DP-2018-028, CERN, Jun, 2018.

[56] CMS Collaboration, "Interpretation of searches for supersymmetry with simplified models", *Phys. Rev. D* **88** (2013), no. 5, 052017, doi:10.1103/PhysRevD.88.052017, arXiv:1301.2175.

[57] W. Beenakker et al., "NNLL-fast: predictions for coloured supersymmetric particle production at the LHC with threshold and Coulomb resummation", *JHEP* **12** (2016) 133, doi:10.1007/JHEP12(2016)133, arXiv:1607.07741.

[58] W. Beenakker, R. Höpker, M. Spira, and P. M. Zerwas, "Squark and gluino production at hadron colliders", *Nucl. Phys. B* **492** (1997) 51, doi:10.1016/S0550-3213(97)00084-9, arXiv:hep-ph/9610490.

[59] A. Kulesza and L. Motyka, "Threshold resummation for squark-antisquark and gluino-pair production at the LHC", *Phys. Rev. Lett.* **102** (2009) 111802, doi:10.1103/PhysRevLett.102.111802, arXiv:0807.2405.

[60] A. Kulesza and L. Motyka, "Soft gluon resummation for the production of gluino-gluino and squark-antisquark pairs at the LHC", *Phys. Rev. D* **80** (2009) 095004, doi:10.1103/PhysRevD.80.095004, arXiv:0905.4749.

[61] W. Beenakker et al., "Soft-gluon resummation for squark and gluino hadroproduction", *JHEP* **12** (2009) 041, doi:10.1088/1126-6708/2009/12/041, arXiv:0909.4418.

[62] W. Beenakker et al., "Squark and gluino hadroproduction", *Int. J. Mod. Phys. A* **26** (2011) 2637, doi:10.1142/S0217751X11053560, arXiv:1105.1110.

[63] CMS Collaboration, "CMS luminosity measurements for the 2016 data taking period", CMS Physics Analysis Summary CMS-PAS-LUM-17-001, CERN, 2017.

[64] CMS Collaboration, "CMS luminosity measurement for the 2017 data-taking period at $\sqrt{s} = 13$ TeV", CMS Physics Analysis Summary CMS-PAS-LUM-17-004, CERN, 2018.

[65] LEP2 SUSY Working Group, ALEPH, DELPHI, L3 and OPAL experiments, "Combined LEP Chargino Results, up to 208 GeV for low DM". http://lepsusy.web.cern.ch/lepsusy/www/inoslowdmsummer02/charginolowdm_pub.html.

A Disappearing track selection

The detailed selection of disappearing tracks (ST and STC) is summarized in Table 3.

Table 3: Selection requirements for *short tracks* (ST) and *short track candidates* (STC). For the subset of medium length (M) tracks that have just four tracking layers with a measurement, the minimum required number of layers of the pixel tracking detector with a measurement is three (†). The selected tracks are required to not overlap with identified leptons. For this selection, all electrons and muons are considered, either identified as PF candidates or not. The selected tracks are as well required to not be identified as PF candidates. The factor by which the selection requirement is relaxed in order to select *short track candidates* is also reported. If no factor is reported, the requirement is not relaxed for the selection of *short track candidates*.

Observable	Selection	Track length	STC factor
p_T [GeV]	> 15	All	
$\lvert\eta\rvert$	< 2.4 and not $1.38 < \lvert\eta\rvert < 1.6$	All	
$\sigma(p_T)$ / p_T^2 [GeV^{-1}]	< 0.2; < 0.02; < 0.005	P; M; L	$\times 3$
d_{xy} (from primary vertex) [cm]	< 0.02 (< 0.01)	P (M, L)	$\times 3$
d_z (from primary vertex) [cm]	< 0.05	All	$\times 3$
Neutral isolation ($\Delta R < 0.05$) [GeV]	< 10	All	$\times 6$
Neutral isolation / p_T	< 0.1	All	$\times 6$
Isolation ($\Delta R < 0.3$) [GeV]	< 10	All	$\times 6$
Isolation / p_T	< 0.2	All	$\times 6$
Number of pixel layers	≥ 3 (≥ 2)	P, M† (M, L)	
Number of lost inner hits	$= 0$	All	
Number of lost outer hits	≥ 2	M, L	
Is a PF candidate?	No	All	
PF lepton veto ($\Delta R < 0.1$)	Yes	All	
Lepton veto ($\Delta R < 0.2$)	Yes	All	
Bad calorimeter module veto	Yes	All	
M_T (track, $\vec{p}_T^{\,\text{miss}}$) [GeV]	> 100, if $p_T < 150$ GeV	L	

B Definition of search regions

B.1 Inclusive M_{T2} search: search regions

The 282 exclusive search regions are defined in Tables 4–6.

Table 4: Summary of signal regions for the monojet selection.

N_{b}	Jet p_{T} binning [GeV]
0	[250, 350, 450, 575, 700, 1000, 1200, ∞)
≥ 1	[250, 350, 450, 575, 700, ∞)

Table 5: The M_{T2} binning in each topological region of the multi-jet search regions, for the very low, low and medium H_T regions.

H_T range [GeV]	Jet multiplicities	M_{T2} binning [GeV]
[250, 450)	$2-3$j, 0b	[200, 300, 400, ∞)
	$2-3$j, 1b	[200, 300, 400, ∞)
	$2-3$j, 2b	[200, 300, 400, ∞)
	$4-6$j, 0b	[200, 300, 400, ∞)
	$4-6$j, 1b	[200, 300, 400, ∞)
	$4-6$j, 2b	[200, 300, 400, ∞)
	≥ 7j, 0b	[200, 300, 500, ∞)
	≥ 7j, 1b	[200, 300, ∞)
	≥ 7j, 2b	[200, 300, ∞)
	$2-6$j, ≥ 3b	[200, 300, 400, ∞)
	≥ 7j, ≥ 3b	[200, 300, ∞)
[450, 575)	$2-3$j, 0b	[200, 300, 400, 500, ∞)
	$2-3$j, 1b	[200, 300, 400, 500, ∞)
	$2-3$j, 2b	[200, 300, 400, 500, ∞)
	$4-6$j, 0b	[200, 300, 400, 500, ∞)
	$4-6$j, 1b	[200, 300, 400, 500, ∞)
	$4-6$j, 2b	[200, 300, 400, 500, ∞)
	≥ 7j, 0b	[200, 300, 400, ∞)
	≥ 7j, 1b	[200, 300, 400, ∞)
	≥ 7j, 2b	[200, 300, 400, ∞)
	$2-6$j, ≥ 3b	[200, 300, 400, 500, ∞)
	≥ 7j, ≥ 3b	[200, 300, 400, ∞)
[575, 1200)	$2-3$j, 0b	[200, 300, 400, 500, 600, 700, 800, 900, 1000, 1100, ∞)
	$2-3$j, 1b	[200, 300, 400, 600, 800, 1000, ∞)
	$2-3$j, 2b	[200, 300, 400, 600, 800, ∞)
	$4-6$j, 0b	[200, 300, 400, 500, 600, 700, 800, 900, 1000, 1100, ∞)
	$4-6$j, 1b	[200, 300, 400, 600, 800, 1000, ∞)
	$4-6$j, 2b	[200, 300, 400, 600, 800, ∞)
	$2-6$j, ≥ 3b	[200, 300, 400, 600, 800, ∞)
	$7-9$j, 0b	[200, 300, 400, 600, 800, ∞)
	$7-9$j, 1b	[200, 300, 400, 600, 800, ∞)
	$7-9$j, 2b	[200, 300, 400, 600, 800, ∞)
	$7-9$j, 3b	[200, 300, 400, 600, ∞)
	$7-9$j, ≥ 4b	[200, 300, 400, ∞)
	≥ 10j, 0b	[200, 300, 500, ∞)
	≥ 10j, 1b	[200, 300, 500, ∞)
	≥ 10j, 2b	[200, 300, 500, ∞)
	≥ 10j, 3b	[200, 300, ∞)
	≥ 10j, ≥ 4b	[200, ∞)

Table 6: The M_{T2} binning in each topological region of the multi-jet search regions, for the high and extreme H_T regions.

H_T range [GeV]	Jet multiplicities	M_{T2} binning [GeV]
[1200, 1500)	$2-3$j, 0b	[200, 400, 600, 800, 1000, 1200, ∞)
	$2-3$j, 1b	[200, 400, 600, 800, 1000, 1200, ∞)
	$2-3$j, 2b	[200, 400, 600, 800, 1000, ∞)
	$4-6$j, 0b	[200, 400, 600, 800, 1000, 1200, ∞)
	$4-6$j, 1b	[200, 400, 600, 800, 1000, 1200, ∞)
	$4-6$j, 2b	[200, 400, 600, 800, 1000, ∞)
	$2-6$j, $\geq$ 3b	[200, 400, 600, ∞)
	$7-9$j, 0b	[200, 400, 600, 800, 1000, ∞)
	$7-9$j, 1b	[200, 400, 600, 800, 1000, ∞)
	$7-9$j, 2b	[200, 400, 600, 800, ∞)
	$7-9$j, 3b	[200, 400, 600, ∞)
	$7-9$j, $\geq$ 4b	[200, 400, ∞)
	$\geq$ 10j, 0b	[200, 400, 600, ∞)
	$\geq$ 10j, 1b	[200, 400, 600, ∞)
	$\geq$ 10j, 2b	[200, 400, 600, ∞)
	$\geq$ 10j, 3b	[200, 400, ∞)
	$\geq$ 10j, $\geq$ 4b	[200, ∞)
[1500, ∞)	$2-3$j, 0b	[400, 600, 800, 1000, 1200, 1400, 1800, ∞)
	$2-3$j, 1b	[400, 600, 800, 1000, 1200, ∞)
	$2-3$j, 2b	[400, ∞)
	$4-6$j, 0b	[400, 600, 800, 1000, 1200, 1400, 1600, ∞)
	$4-6$j, 1b	[400, 600, 800, 1000, 1400, ∞)
	$4-6$j, 2b	[400, 600, 800, ∞)
	$2-6$j, $\geq$ 3b	[400, 600, ∞)
	$7-9$j, 0b	[400, 600, 800, 1000, 1400, ∞)
	$7-9$j, 1b	[400, 600, 800, ∞)
	$7-9$j, 2b	[400, 600, 800, ∞)
	$7-9$j, 3b	[400, 800, ∞)
	$7-9$j, $\geq$ 4b	[400, ∞)
	$\geq$ 10j, 0b	[400, 800, ∞)
	$\geq$ 10j, 1b	[400, 800, ∞)
	$\geq$ 10j, 2b	[400, ∞)
	$\geq$ 10j, 3b	[400, ∞)
	$\geq$ 10j, $\geq$ 4b	[400, ∞)

B.2 Search for disappearing tracks: search regions

The 68 search regions are defined in Tables 7–8.

Table 7: Summary of the signal regions of the search for disappearing tracks, for the 2016 data set.

Track length	N_j	H_T range [GeV]	Track p_T [GeV]	Label
P	2–3	[250, 450)	[15, 50)	P LL lo
			[50, ∞)	P LL hi
		[450, 1200)	[15, 50)	P LM lo
			[50, ∞)	P LM hi
		[1200, ∞)	[15, 50)	P LH lo
			[50, ∞)	P LH hi
	≥ 4	[250, 450)	[15, 50)	P HL lo
			[50, ∞)	P HL hi
		[450, 1200)	[15, 50)	P HM lo
			[50, ∞)	P HM hi
		[1200, ∞)	[15, 50)	P HH lo
			[50, ∞)	P HH hi
M	2–3	[250, 450)	[15, 50)	M LL lo
			[50, ∞)	M LL hi
		[450, 1200)	[15, 50)	M LM lo
			[50, ∞)	M LM hi
		[1200, ∞)	[15, 50)	M LH lo
			[50, ∞)	M LH hi
	≥ 4	[250, 450)	[15, 50)	M HL lo
			[50, ∞)	M HL hi
		[450, 1200)	[15, 50)	M HM lo
			[50, ∞)	M HM hi
		[1200, ∞)	[15, 50)	M HH lo
			[50, ∞)	M HH hi
L	2–3	[250, 1200)	[15, ∞)	L LLM
		[1200, ∞)	[15, ∞)	L LH
	≥ 4	[250, 1200)	[15, ∞)	L HLM
		[1200, ∞)	[15, ∞)	L HH

Table 8: Summary of the signal regions of the search for disappearing tracks, for the 2017–2018 data set.

Track length	N_j	H_T range [GeV]	Track p_T [GeV]	Label
P3	2–3	[250, 450)	[15, 50)	P3 LL lo
			[50, ∞)	P3 LL hi
		[450, 1200)	[15, 50)	P3 LM lo
			[50, ∞)	P3 LM hi
		[1200, ∞)	[15, 50)	P3 LH lo
			[50, ∞)	P3 LH hi
	≥ 4	[250, 450)	[15, 50)	P3 HL lo
			[50, ∞)	P3 HL hi
		[450, 1200)	[15, 50)	P3 HM lo
			[50, ∞)	P3 HM hi
		[1200, ∞)	[15, 50)	P3 HH lo
			[50, ∞)	P3 HH hi
P4	2–3	[250, 450)	[15, 50)	P4 LL lo
			[50, ∞)	P4 LL hi
		[450, 1200)	[15, 50)	P4 LM lo
			[50, ∞)	P4 LM hi
		[1200, ∞)	[15, 50)	P4 LH lo
			[50, ∞)	P4 LH hi
	≥ 4	[250, 450)	[15, 50)	P4 HL lo
			[50, ∞)	P4 HL hi
		[450, 1200)	[15, 50)	P4 HM lo
			[50, ∞)	P4 HM hi
		[1200, ∞)	[15, 50)	P4 HH lo
			[50, ∞)	P4 HH hi
M	2–3	[250, 450)	[15, 50)	M LL lo
			[50, ∞)	M LL hi
		[450, 1200)	[15, 50)	M LM lo
			[50, ∞)	M LM hi
		[1200, ∞)	[15, 50)	M LH lo
			[50, ∞)	M LH hi
	≥ 4	[250, 450)	[15, 50)	M HL lo
			[50, ∞)	M HL hi
		[450, 1200)	[15, 50)	M HM lo
			[50, ∞)	M HM hi
		[1200, ∞)	[15, 50)	M HH lo
			[50, ∞)	M HH hi
L	2–3	[250, 1200)	[15, ∞)	L LLM
		[1200, ∞)	[15, ∞)	L LH
	≥ 4	[250, 1200)	[15, ∞)	L HLM
		[1200, ∞)	[15, ∞)	L HH

C Detailed results

C.1 Inclusive M_{T2} search: pre-fit background

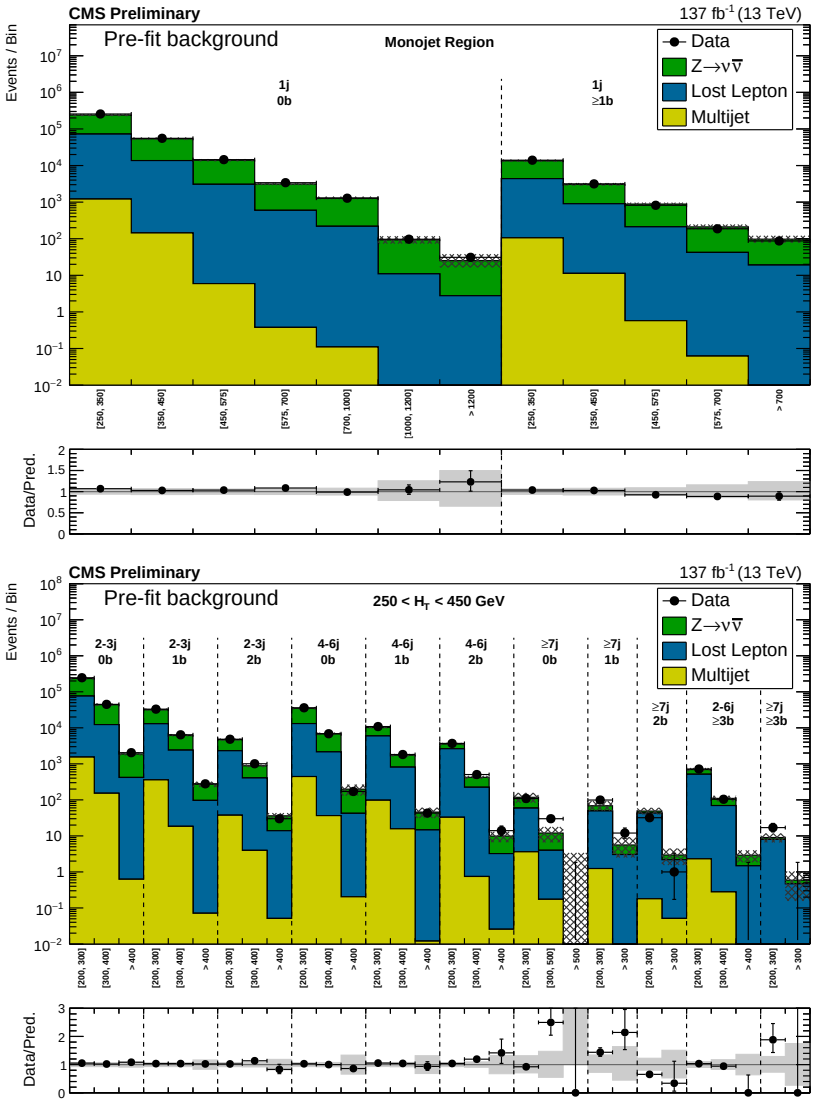

Figure 12: (Upper) Comparison of the estimated background and observed data events in each signal bin in the monojet region. On the x-axis, the $p_{\mathrm{T}}^{\mathrm{jet1}}$ binning is shown in units of GeV. Hatched bands represent the full uncertainty in the background estimate. The notations j, b indicate N_{j}, N_{b} labeling. (Lower) Same for the very low H_{T} region. On the x-axis, the M_{T2} binning is shown in units of GeV.

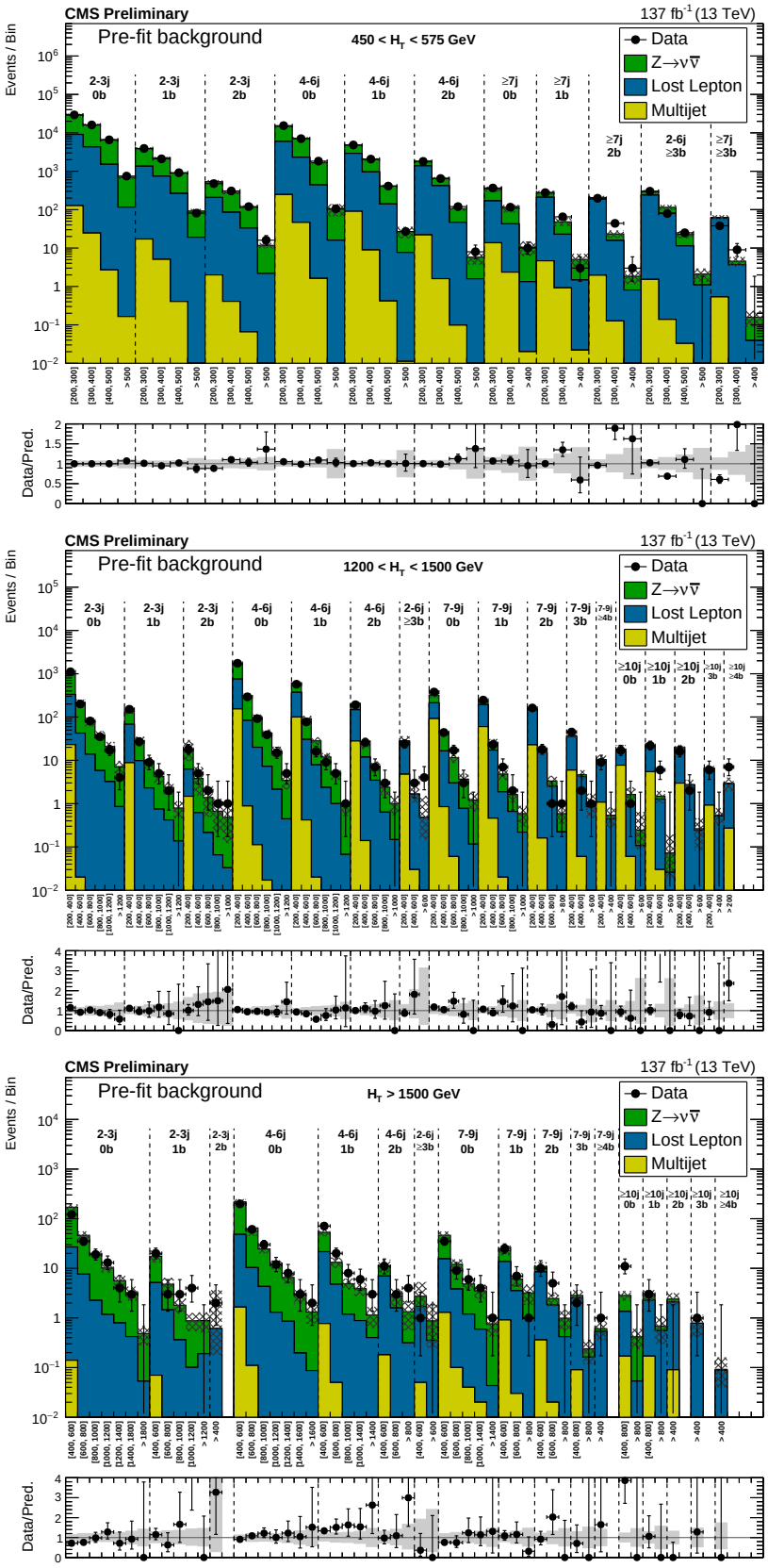

Figure 13: (Upper) Comparison of the estimated background and observed data events in each signal bin in the low-H_T region. Hatched bands represent the full uncertainty in the background estimate. The notations j, b indicate N_j, N_b labeling. Same for the high- (middle) and extreme- (lower) H_T regions. On the x-axis, the M_{T2} binning is shown in units of GeV.

C.2 Inclusive M_{T2} search: post-fit background

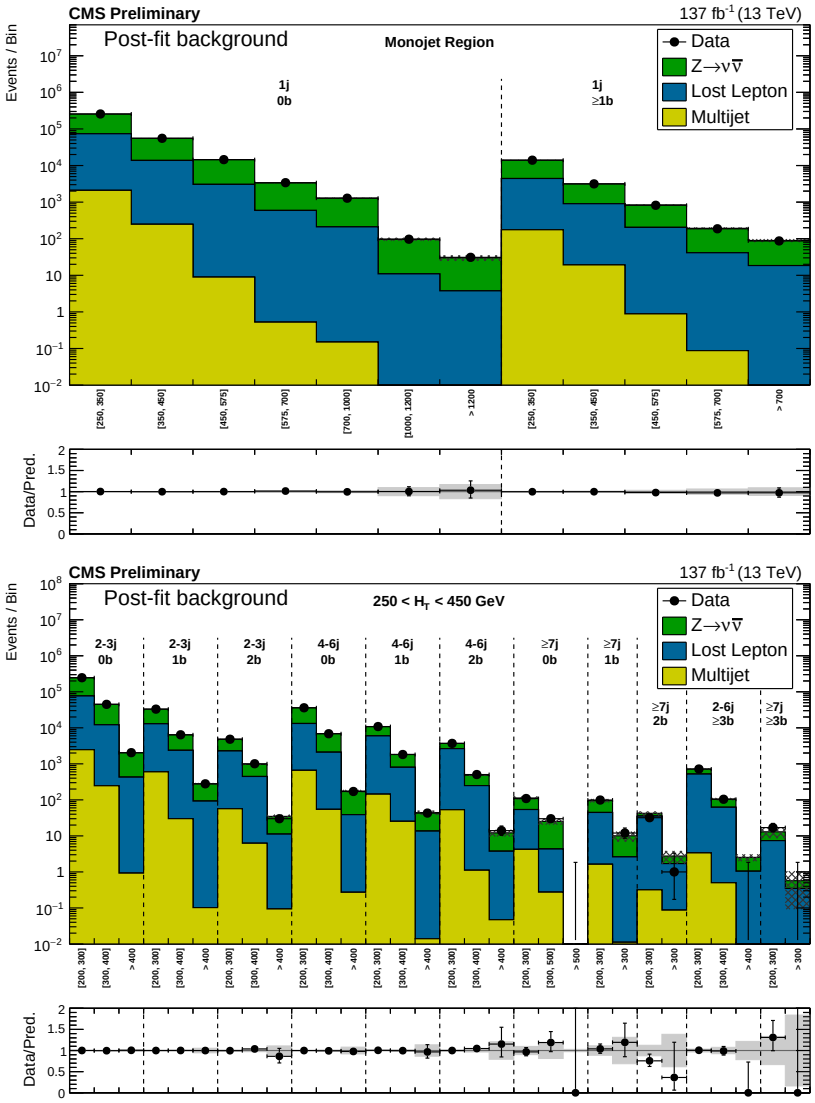

Figure 14: (Upper) Comparison of the *post-fit* estimated background and observed data events in each signal bin in the monojet region. On the x-axis, the $p_{\mathrm{T}}^{\mathrm{jet1}}$ binning is shown in units of GeV. Hatched bands represent the full uncertainty in the background estimate. The notations j, b indicate N_{j}, N_{b} labeling. (Lower) Same for the very low-H_{T} region. On the x-axis, the M_{T2} binning is shown in units of GeV.

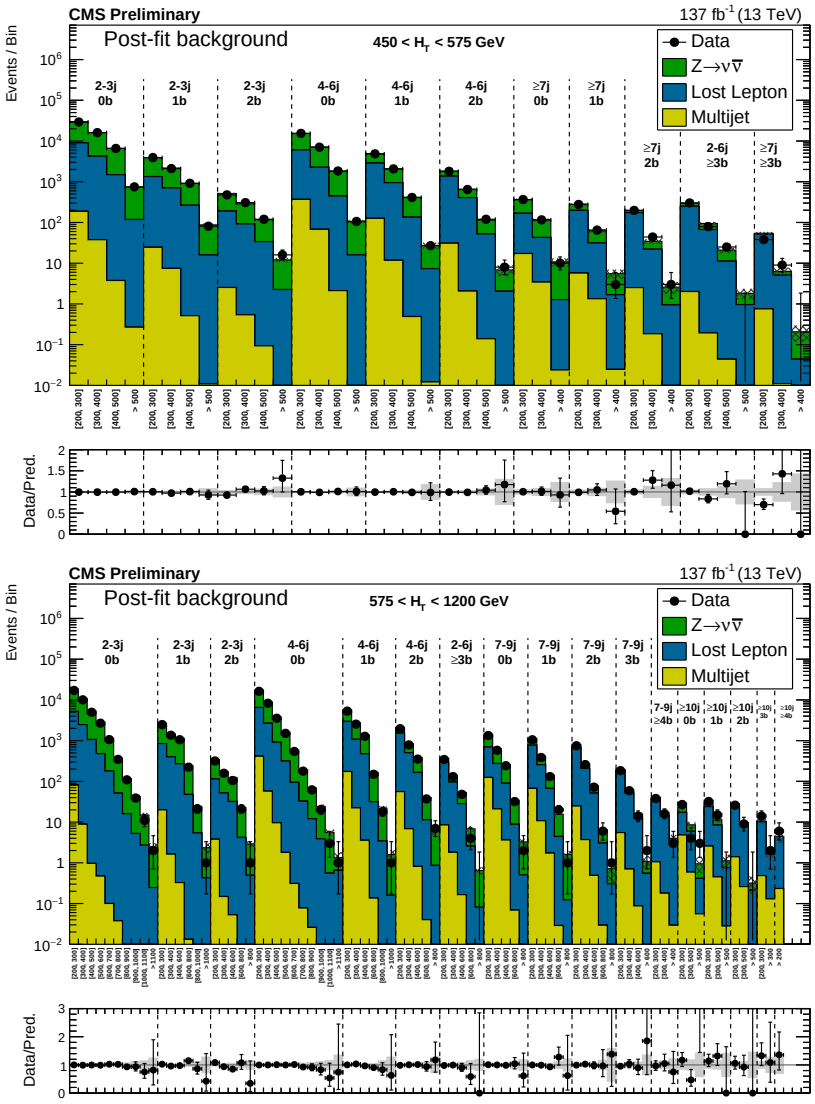

Figure 15: (Upper) Comparison of the *post-fit* estimated background and observed data events in each signal bin in the low-H_T region. Hatched bands represent the full uncertainty in the background estimate. The notations j, b indicate N_j, N_b labeling. (Lower) Same for the medium-H_T region. On the x-axis, the M_{T2} binning is shown in units of GeV.

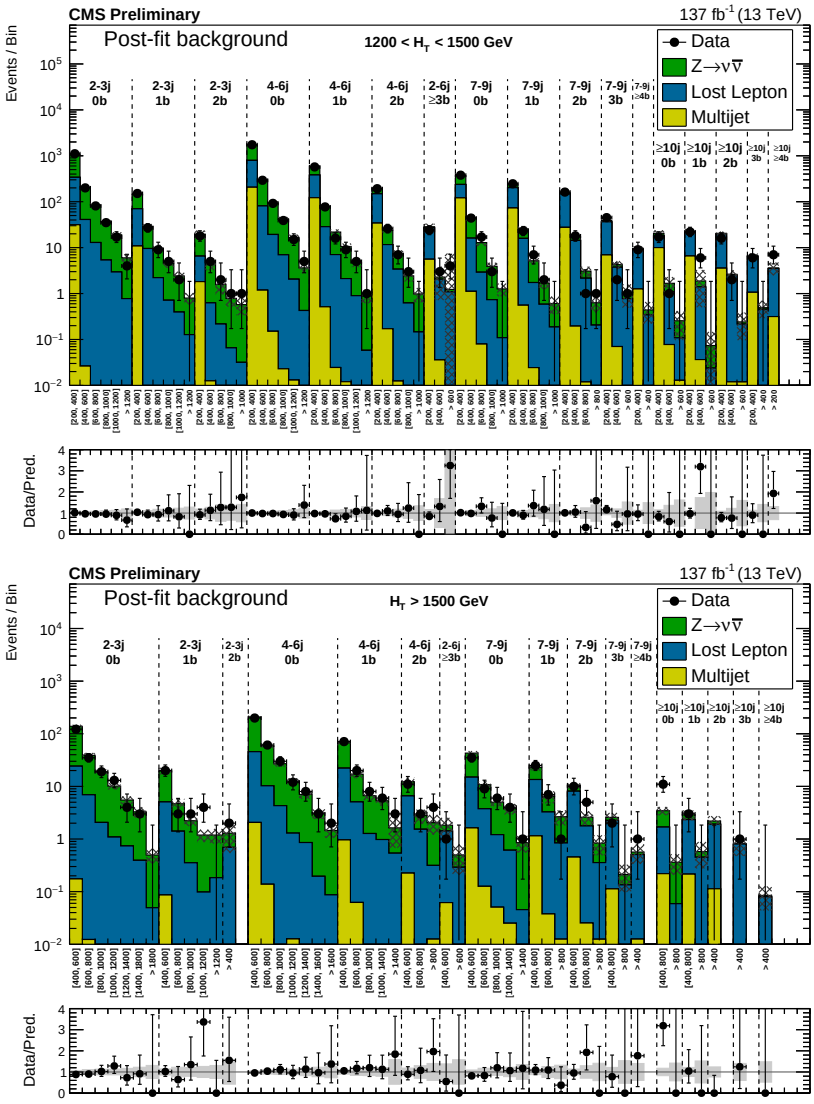

Figure 16: (Upper) Comparison of the *post-fit* estimated background and observed data events in each signal bin in the high-H_{T} region. Hatched bands represent the full uncertainty in the background estimate. The notations j, b indicate N_{j}, N_{b} labeling. (Lower) Same for the extreme-H_{T} region. On the x-axis, the M_{T2} binning is shown in units of GeV.

C.3 Search for disappearing tracks: post-fit background

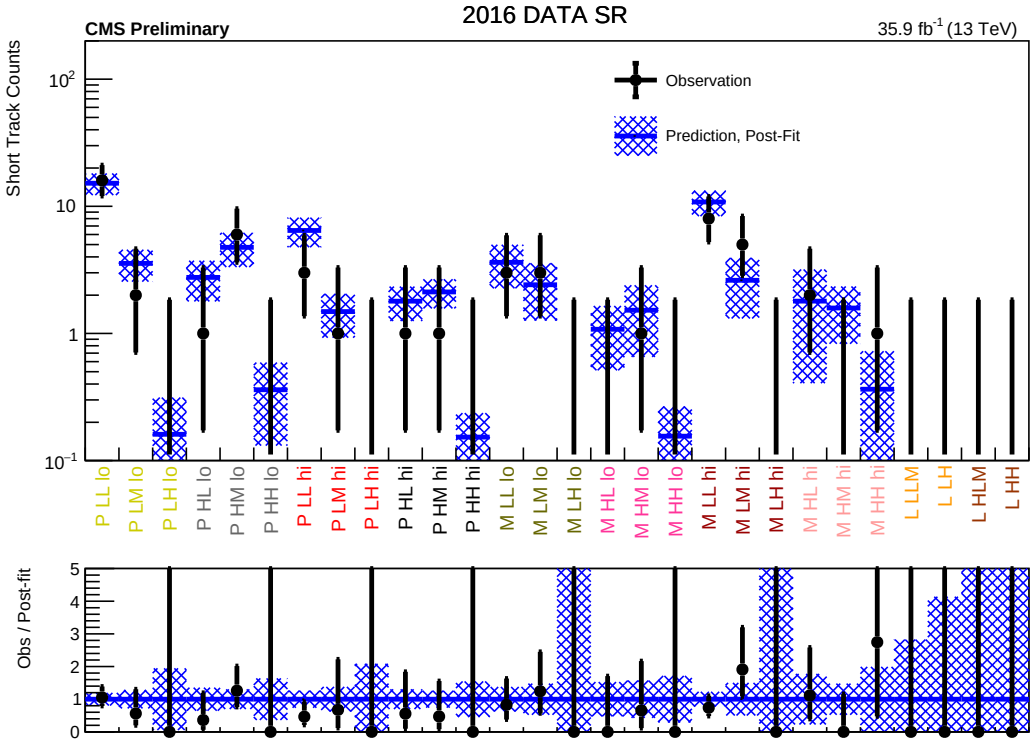

Figure 17: Background prediction (*post-fit*) and observation in the 2016 data signal region, in the full analysis binning of the search for disappearing tracks. The blue histogram represents the predicted (*post-fit*) background, while the black points are the actual observed data counts. The blue band represents the uncertainty on the prediction. The labels on the x-axes are explained in Tables 7–8 of Appendix B.2. Regions whose predictions use the same measurement of f_{short} are identified by the colors of the labels.

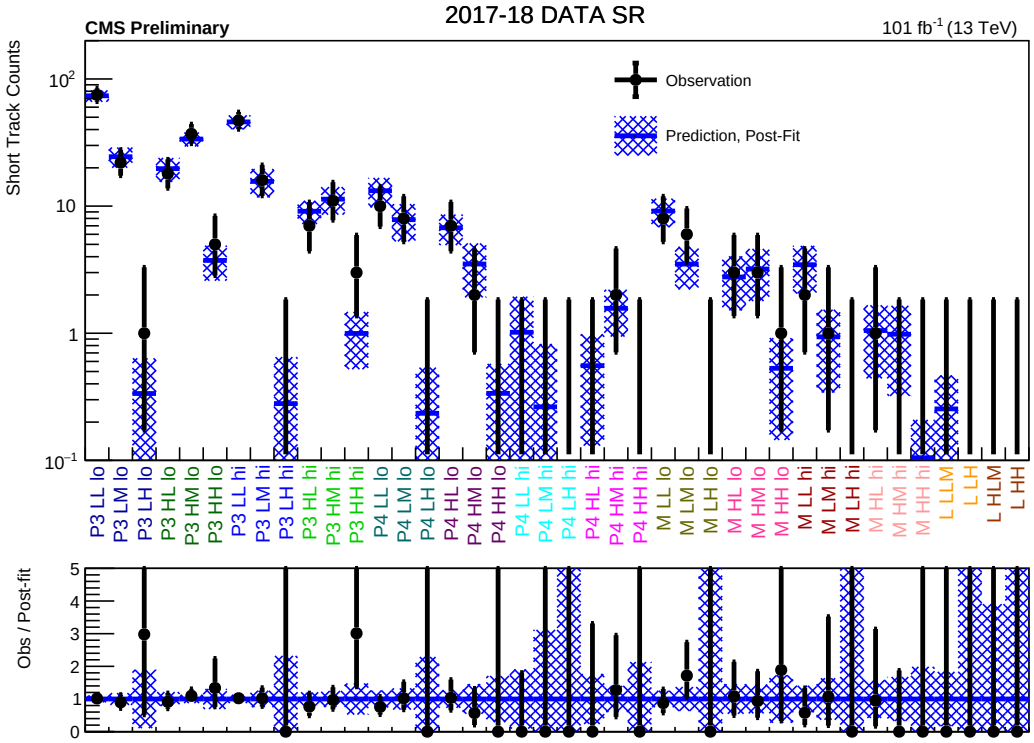

Figure 18: Background prediction (*post-fit*) and observation in the 2017–2018 data signal region, in the full analysis binning of the search for disappearing tracks. The blue histogram represents the predicted (*post-fit*) background, while the black points are the actual observed data counts. The blue band represents the uncertainty on the prediction. The labels on the x-axes are explained in Tables 7–8 of Appendix B.2. Regions whose predictions use the same measurement of f_{short} are identified by the colors of the labels.